

A fully-automatic method to segment the carotid artery layers in ultrasound imaging – Application to quantify the compression-decompression pattern of the intima-media complex during the cardiac cycle

Guillaume Zahnd^{a,*}, Kostas Kapellias^b, Martijn van Hattem^c, Anouk van Dijk^c, André Sérusclat^d, Philippe Moulin^e, Aad van der Lugt^c, Michael Skilton^f, Maciej Orkisz^g

^a*Biomedical Imaging Group Rotterdam, Departments of Radiology & Nuclear Medicine and Medical Informatics, Erasmus MC, University Medical Center Rotterdam, Rotterdam, The Netherlands*

^b*Australian Research Centre for Population Oral Health, School of Dentistry, University of Adelaide, Adelaide, Australia*

^c*Department of Radiology, Erasmus MC, University Medical Center Rotterdam, Rotterdam, the Netherlands*

^d*Department of Radiology, Louis Pradel Hospital; Hospices Civils de Lyon; Université Lyon 1, Lyon, France*

^e*Department of Endocrinology, Louis Pradel Hospital; Hospices Civils de Lyon; Université Lyon 1, Lyon, France*

^f*Boden Institute of Obesity, Nutrition, Exercise and Eating Disorders, University of Sydney*

^g*Univ Lyon, INSA-Lyon, Université Lyon 1, UJM-Saint Etienne, CNRS, Inserm, CREATIS UMR 5220, U1206, F-69621, Lyon, France*

*This manuscript has been published in **Ultrasound in Medicine and Biology** 43(1):239-257, 2016. The final version is available at: <http://dx.doi.org/10.1016/j.ultrasmedbio.2016.08.016>*

Abstract

The aim of this study was to introduce and evaluate a contour segmentation method to extract the interfaces of the intima-media complex in carotid B-mode ultrasound

*Corresponding author

E-mail: g.zahnd@erasmusmc.nl

Address: Biomedical Imaging Group Rotterdam, Erasmus MC, P.O. Box 2040, 3000 CA Rotterdam, the Netherlands

Telephone: +31-10-7043050

images. The method was applied to assess the temporal variation of the intima-media thickness during the cardiac cycle.

The main methodological contribution of the proposed approach is the introduction of an augmented dimension to process two-dimensional images in a three-dimensional space. The third dimension, which is added to the two spatial dimensions of the image, corresponds to the tentative local thickness of the intima-media complex. The method is based on a dynamic programming scheme that runs in a three-dimensional space generated with a shape-adapted filter bank. The optimal solution corresponds to a single medial axis representation that fully describes the two anatomical interfaces of the arterial wall. The method is fully-automatic and does not require any input from the user.

The method was trained on 60 subjects and validated on 184 other subjects from six different cohorts and four different medical centers. The arterial wall was successfully segmented in all analyzed images (average pixel size of $57 \pm 20 \mu\text{m}$), with average segmentation errors of $47 \pm 70 \mu\text{m}$ for the lumen-intima interface, $55 \pm 68 \mu\text{m}$ for the media-adventitia interface, and $66 \pm 90 \mu\text{m}$ for the intima-media thickness. The amplitude of the temporal variations in IMT during the cardiac cycle was significantly higher in the diseased population compared to healthy volunteers (106 ± 48 vs. $86 \pm 34 \mu\text{m}$, $p = 0.001$).

The introduced framework is a promising approach to investigate an emerging functional parameter of the arterial wall, by assessing the cyclic compression-decompression pattern of the tissues.

Keywords: Contour segmentation, Carotid artery, Ultrasound, Dynamic programming, Front propagation, Intima-media thickness

1 Introduction

2 Cardiovascular diseases are the leading cause of mortality and morbidity world-
3 wide (WHO, 2015). An early sign of the atherosclerotic process is arterial wall
4 thickening. Carotid intima-media thickness (IMT, Fig. 1) has been demonstrated
5 to be strongly correlated with cardiovascular diseases (O’Leary et al., 1999; Baldas-
6 sarre et al., 2000; Polak et al., 2011), and is considered an established biomarker
7 of atherosclerosis (Lorenz et al., 2007): IMT values < 1.1 mm indicate a healthy
8 artery (Jarauta et al., 2010), values > 1.5 mm are a surrogate marker for an atheroscle-
9 rosis plaque (Touboul et al., 2012), and transitional values define an intermediate
10 risk. Therefore, assessing IMT is crucial to evaluate the cardiovascular risk. The fo-
11 cus of the present study is the assessment of IMT at an early stage of atherosclerosis,
12 in images without atheromatous plaque.

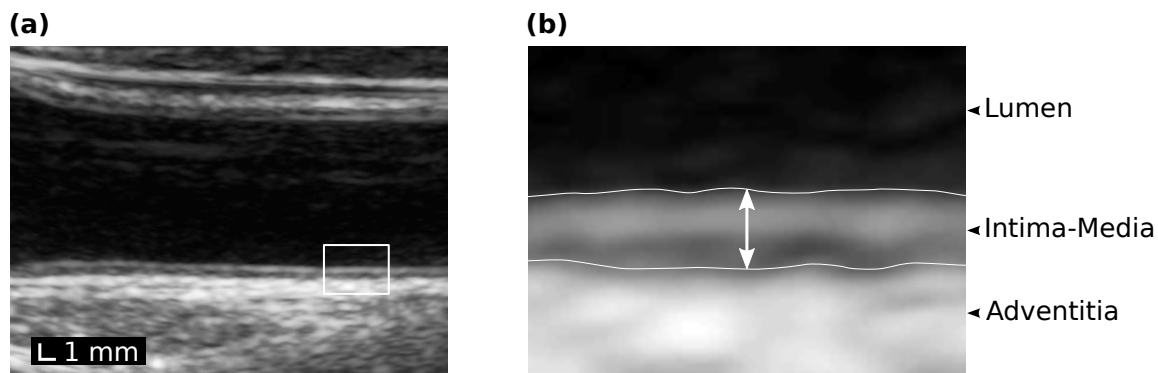


Figure 1: (a) Longitudinal view of the common carotid artery in B-mode ultrasound imaging. (b) Enlarged region detailing the intima-media complex. The lumen-intima and media-adventitia interfaces are represented by the contour lines, and the intima-media thickness is indicated by the arrow.

13 B-mode ultrasound (US) imaging has been extensively used to assess carotid IMT
 14 *in vivo*. The problem of quantifying the IMT is generally addressed by extracting the
 15 two contours of the intima-media complex – *i.e.*, the lumen-intima (LI) and media-
 16 adventitia (MA) interfaces, Figure 1 –, and calculating the distance between these
 17 two contours. According to the Mannheim consensus (Touboul et al., 2012), the far
 18 wall of the artery is generally analyzed, mainly due to better depiction of the intima-
 19 media double-line pattern, and to possible overestimation of the IMT in the near
 20 wall (Skilton et al., 2011). A large number of computerized segmentation methods
 21 have been proposed to (semi-) automatically extract the LI and MA interfaces in two-
 22 dimensional (2D) US images. Recent comprehensive review articles (Molinari et al.,
 23 2010; Ilea et al., 2013; Loizou, 2014) propose categorizations of these methods ac-
 24 cording to image-processing techniques used, and provide their synthetic description
 25 together with main results, etc. Hereafter, we cite only examples of major studies.

26 Let us note that the interfaces of interest may be extracted either sequentially or
 27 simultaneously. Most of the existing methods fall in the broad category of sequential
 28 contour extraction, *i.e.*, the two contours are extracted more or less independently
 29 (sometimes one extracted contour being used as initialization to extract the second
 30 one), and then possibly refined to improve their spatial consistency. Among these
 31 approaches, methods based on feature extraction and region classification have been
 32 recommended to extract the pixels that belong to the intima-media complex (Moli-
 33 nari et al., 2011; Menchón-Lara et al., 2014). An edge operator based on statistical

34 filtering has been introduced to extract the anatomical boundaries by analyzing the
35 local statistics of the image (Faita et al., 2008). A method based on adaptive
36 thresholding followed by a morphological operation was proposed to detect the con-
37 tours of the layers (Ilea et al., 2013). Various implementations of the active-contour
38 framework have been put forward by different teams (Mao et al., 2000; Cheng et al.,
39 2002; Loizou et al., 2007; Xu et al., 2012; Bastida-Jumilla et al., 2015). Dynamic
40 programming methodology has also been adopted in combination with various tech-
41 niques, such as fuzzy expression forms representing image features and geometrical
42 characteristics of vessel-wall interfaces (Liang et al., 2000), smooth intensity thresh-
43 olding surfaces and geometric snakes (Rocha et al., 2010), and directional Haar-like
44 filter (Lee et al., 2010).

45 Cheng and Jiang (2008) proposed a dual-dynamic-programming method control-
46 ling the simultaneous evolution of two curves and devised to jointly extract both
47 contours of the intima-media complex. They argued that their approach was able to
48 robustly cope with noise and irregular contrasts. In particular, the article demon-
49 strated that dual dynamic programming was more efficient in handling the spatial
50 consistency of the contours than traditional dynamic programming, where the con-
51 tours, extracted sequentially, may intersect or collapse onto each other. Following
52 a similar strategy, we have developed a method (Zahnd et al., 2012, 2013b) based
53 on a representation known as *medial axis*, *i.e.*, a single object fully describing the
54 two contours of the intima-media complex by means of *i)* the radial *position* of a
55 curve located mid-way between LI and MA interfaces, and *ii)* the local *distance* be-
56 tween each contour and this curve. That information was separately estimated in
57 each column of the image by means of a shape-adapted filter bank. The algorithm
58 processed a whole image sequence (hereafter referred to as *cine-loop*) after an inter-
59 active initialization performed in the first frame. The method efficiently controlled
60 the location and smooth shape of the central curve, but could not guarantee the
61 smoothness of the contours.

62 Overall, accuracy of the methods reported by the above-cited studies, in IMT
63 quantification, as well as in both LI and MA interfaces extraction, ranged between 10
64 and 90 μm . Nevertheless, these results were obtained using different images, distinct
65 reference annotations, and possibly not the same evaluation protocols. According to
66 recent surveys (Molinari et al., 2010; Ilea et al., 2013; Loizou, 2014), for the majority
67 of the studies available in the literature, evaluation was carried out using a relatively
68 limited number (typically, below 50) of images that were generally acquired using
69 only one scanner. Additionally, in most of these studies, training data were not
70 specified; if the same images were used to tune a method and determine its optimal
71 parameter settings, and then to evaluate it, the robustness of this methods with

72 respect to new data and scanners may be questionable. Moreover, although some
73 approaches are fully automatic (Molinari et al., 2011; Ilea et al., 2013; Menchón-
74 Lara et al., 2014; Bastida-Jumilla et al., 2015), the majority of the existing methods
75 require manual input from the user. Such user interaction, which can range from
76 several mouse-clicks to interactive parameter tuning, may be necessary to overcome
77 various difficulties, *e.g.*, related to acquisition-specific variability, but it is known
78 to introduce inter- and intra-observer variability, when dealing with the same case,
79 while automatic methods are fully reproducible, when applied to the same data.
80 Additionally, to limit the user’s workload, methods devised for cine-loops containing
81 hundred frames or more must be maximally automated.

82 The aim of the present study was to develop a fully automatic method capa-
83 ble of simultaneously extracting both contours of the intima-media complex, in US
84 cine loops, with sufficient accuracy to quantify minute variations of IMT during the
85 cardiac cycle. To this purpose, we introduced a dynamic-programming algorithm
86 that conducts a minimum-cost-path search in a three-dimensional (3D) space built
87 of the two spatial dimensions (width and height) of the image, and of all potential
88 IMT values. The minimum-cost-path defines a smooth 3D medial axis that describes
89 the spatial location and shape of the intima-media complex, as well as its thickness
90 in each column of the image. A fully-automatic framework is presented to run the
91 method without any user interaction. Nevertheless, the user may choose to manually
92 perform part or all of the otherwise automatic initialization phase.

93 The introduced contour segmentation method was first trained on a subset of
94 *in vivo* data corresponding to 60 subjects from four different cohorts provided by
95 three medical centers, then it was validated on a set of *in vivo* data with variable
96 image characteristics and quality, corresponding to 184 subjects from six distinct
97 cohorts, imaged with different scanners in four medical centers. Furthermore, as
98 the amplitude Δ_{IMT} of the temporal variations in IMT during the cardiac cycle
99 has been demonstrated to be associated with cardiovascular risk factors (Boutouyrie
100 et al., 2001; Meinders et al., 2003; Polak et al., 2012b,a; Zahnd et al., 2013b), the
101 method was finally applied to quantify this emerging and potentially relevant clinical
102 parameter.

103 Methods

104 Similarly to our previous work (Zahnd et al., 2012, 2013b), the contour-extraction
105 method is based on the well-known concept of medial axis. In 2D images, this concept
106 corresponds to a representation of (mainly elongated) objects by a line located in
107 the object half-way between its contours; each point of the line carries information
108 about the distance to the contours. In our implementation, the gap between the
109 contours, designated by the variable Δ , is calculated column-wise; in the sequel, this
110 gap will be referred to as distance or IMT, although it is not rigorously equal to
111 the actual distance calculated in the direction perpendicular to the contour, when
112 the wall is curved or tilted in the image. Figure 2 represents the work-flow of the
113 method applied within a region of interest (ROI) \mathcal{I}_W of a single frame, where W
114 stands for the width of the ROI. The steps of the work-flow will be detailed in the
115 subsequent sections; here we give its outline. The first step (a-b) uses the shape
116 and location of the medial axis from the previous frame (or from the initialization,
117 if the very first frame of the cine loop is considered), in order to “flatten” the region
118 of interest centered on the intima-media complex, so that the contours of the latter
119 become nearly horizontal. In the second step (c), a bank of filters sensitive to the
120 typical two-line pattern of the intima-media complex is applied in each point of
121 the image. The response of a filter is strong if the point, in which it is applied,
122 is located half-way between two edges. Since the IMT can vary spatially and/or
123 temporally (Selzer et al., 2001) each filter in the bank is tuned to a different spacing
124 Δ between edges, and the range of these tentative spacings is set as a function of the
125 IMT value estimated in the previous frame (or provided by the initialization). The
126 responses of the filters form a 3D map, where the first two dimensions correspond to
127 the x and y spatial dimensions in the image, while the third dimension corresponds
128 to the spacing Δ . In the third step (d), filter responses are transformed into costs:
129 stronger responses give rise to lower costs. In the fourth step (e), front propagation is
130 carried out starting from $x = 0$: the front propagates faster where the cost is lower,
131 while its non-horizontal displacements and changes in Δ are penalized. The result
132 of this step is a map of arrival times. In the subsequent step (f), the minimum-cost
133 path is found by a gradient descent in this map. After the last step (g), which applies
134 the inverse transformation with respect to the “flattening”, this path defines a new
135 medial axis, and the next frame can be processed. Let us note that the first step
136 (a-b) was identical in our previous method (Zahnd et al., 2012, 2013b), as well as
137 the filter bank. These will be summarized in the subsection “Background”, whereas
138 the actual contributions of the current work will be described in the subsections
139 “Contour extraction” and “Automatic initialization”.

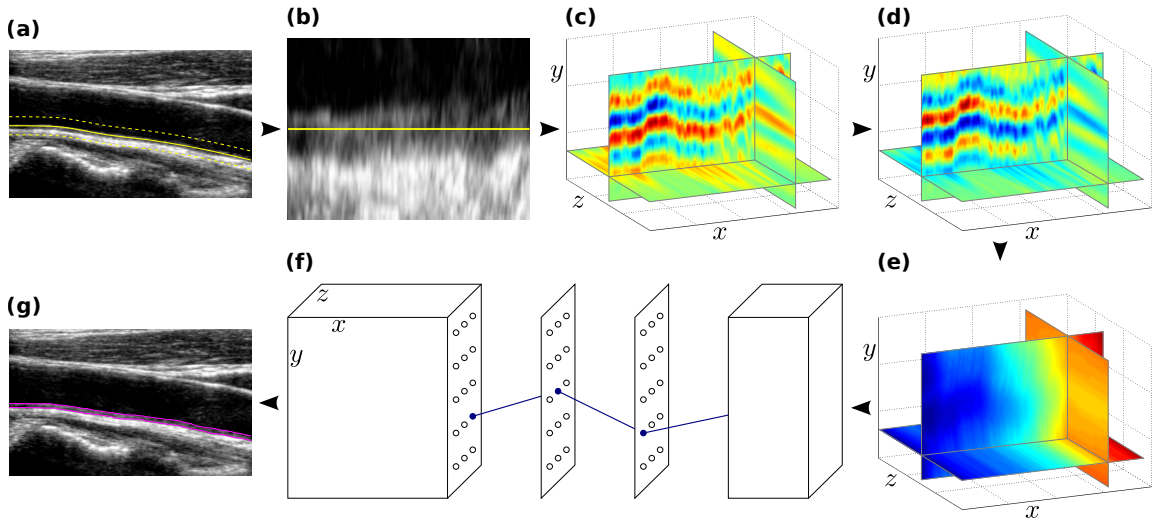


Figure 2: Illustration of the main steps of the segmentation method, applied here to the full width of an image (*i.e.*, $\mathcal{I}_W = \mathcal{I}$ in this example). (a) Initial image \mathcal{I} , with the medial axis from the previous image (solid yellow line). (b) Sub-image \mathcal{I}_T , resulting from the T transformation of the region located between the dashed yellow lines in (a), such that the anatomical interfaces around the previous medial axis (solid yellow line) are nearly horizontal. (c) 3D volume, corresponding to the set of K velocity maps F_{Δ^k} generated with the filter bank \mathcal{H}_{Δ} . (d) 3D cost function \mathcal{C} . (e) 3D cumulative cost function \mathbb{C} corresponding to a left-to-right direction of propagation. (f) Schematic representation of the optimal path (blue line), extracted by backtracking the decreasing values in \mathbb{C} , corresponding to the medial axis: for each column (x), the radial position (y) of the medial axis as well as the local IMT (z) are fully described by the coordinates of the corresponding node. (g) Resulting contour extraction (violet lines) after the inverse T^{-1} transformation.

140 *Background*

141 *Spatial transformation T .* The aim of the transformation T is to generate a sub-
 142 image \mathcal{I}_T , centered around the far wall, in which the anatomical interfaces of possibly
 143 tilted or curved wall become nearly horizontal (Fig. 2a,b). Briefly, the transforma-
 144 tion T consists in mapping the medial axis from the previous frame onto the current
 145 frame, and then selecting, for each column in \mathcal{I}_W , a region of height H centered
 146 around the medial axis, which is assumed to be smooth. This column-by-column
 147 re-sampling is associated with longitudinal smoothing by a Gaussian filter G_{σ_x} of
 148 standard deviation σ_x . The values of H , σ_x , and of all other parameters will be

149 specified in the experimental part.

150 *Filter bank.* The shape-adapted filter \mathcal{H}_Δ introduced in our previous study (Zahnd
151 et al., 2013b) is defined as

$$\mathcal{H}_\Delta = \pm G'_{\sigma_y} * \mathcal{M}_\Delta, \quad (1)$$

152 where $(*)$ is the convolution operator, G'_{σ_y} is the first derivative of a Gaussian with
153 standard deviation σ_y , and \mathcal{M}_Δ is a pair of Diracs separated by a distance Δ . The
154 term G'_{σ_y} alone, convolved with an image, is usually used to calculate the intensity
155 gradient, and thus highlight the edges. Combined with the term \mathcal{M}_Δ , it highlights
156 the expected position of the medial axis, located mid-way between two edges (in our
157 case, LI and MA interfaces) separated by the gap Δ and having the same sign of the
158 gradient. The \pm sign corresponds to the expected gradient orientation: it is negative
159 for the far wall used in this study, and would be positive if the near wall was assessed.
160 Column-wise convolution of the \mathcal{H}_Δ filter with \mathcal{I}_T generates a response F_Δ :

$$F_\Delta = \mathcal{H}_\Delta * \mathcal{I}_T. \quad (2)$$

161 Let us remind that the scope of the present study is early stage atherosclerosis;
162 therefore no atheromatous plaques are present in the image, and the IMT is expected
163 to be almost constant across the image. Nevertheless, the thickness of the layers
164 remains subject to a certain amount of variability that can occur both spatially
165 (*i.e.*, within a single frame) and temporally (*i.e.*, between consecutive frames) (Selzer
166 et al., 2001). To cope with such minute variation of the IMT, a range of different
167 Δ values is assessed. Since the spatial resolution is relatively coarse with respect to
168 the expected IMT variation, the image \mathcal{I}_T is first interpolated by a factor 10 in the
169 radial direction to increase the precision. Then, a set of K filters \mathcal{H}_{Δ^k} is successively
170 applied to \mathcal{I}_T to build K functions F_{Δ^k} . The K tentative values of the local IMT
171 are defined as:

$$\Delta^k = \Delta(n-1) + k\delta, k \in \mathcal{K} \equiv \left\{ -\frac{K-1}{2}, \dots, 0, \dots, \frac{K-1}{2} \right\}, \quad (3)$$

172 where δ is an increment corresponding to the minimal IMT variation investigated,
173 and $\Delta(n-1)$ is the IMT value estimated in the previous image $\mathcal{I}(n-1)$. When
174 $n = 1$, the approximate IMT value found in the initialization step is used. In the
175 current implementation, the range of these tentative values is restricted by threshold
176 values Δ_{MIN} and Δ_{MAX} to discard non-realistic IMT solutions, and thus increase
177 the robustness of the method and avoid a potential divergence during successive
178 time-steps.

179 In the context of front propagation, F_Δ can be interpreted as a velocity function:
180 the front tends to propagate towards the points with larger values of F . Additionally,
181 the propagation is constrained to ensure the smoothness of the resulting minimum-
182 cost path. Before running the front propagation and the subsequent minimum-cost-
183 path search, the velocity function F is transformed into a positive cost function \mathcal{C} ,
184 where small values correspond to strong filter responses:

$$\mathcal{C} = \exp(-F). \quad (4)$$

185 In our previous work, the function F was two-dimensional: it was obtained by se-
186 lecting, for each point of spatial coordinates (x, y) , the largest response among K
187 filters applied in the same point: $F(x, y) = \max_{k \in \mathcal{K}}(F_{\Delta^k}(x, y))$. This blind selection
188 of the maximal output, without fully exploiting the smoothness of the anatomical
189 structures of interest, was the limitation of that method. Indeed, artefactual patterns
190 similar to the actual intima-media complex may produce the strongest filter response
191 for inconsistent spatial locations and Δ values; whereas constraining the front propa-
192 gation by means of a penalty proportional to vertical displacements guaranteed that
193 the radial positions of the medial axis were smooth, there was no smoothness con-
194 straint on the selected Δ values. It was therefore possible to assign highly different Δ
195 values to adjacent columns in the image, thus generating irregular contours despite
196 a smooth medial axis (Fig 3 left).

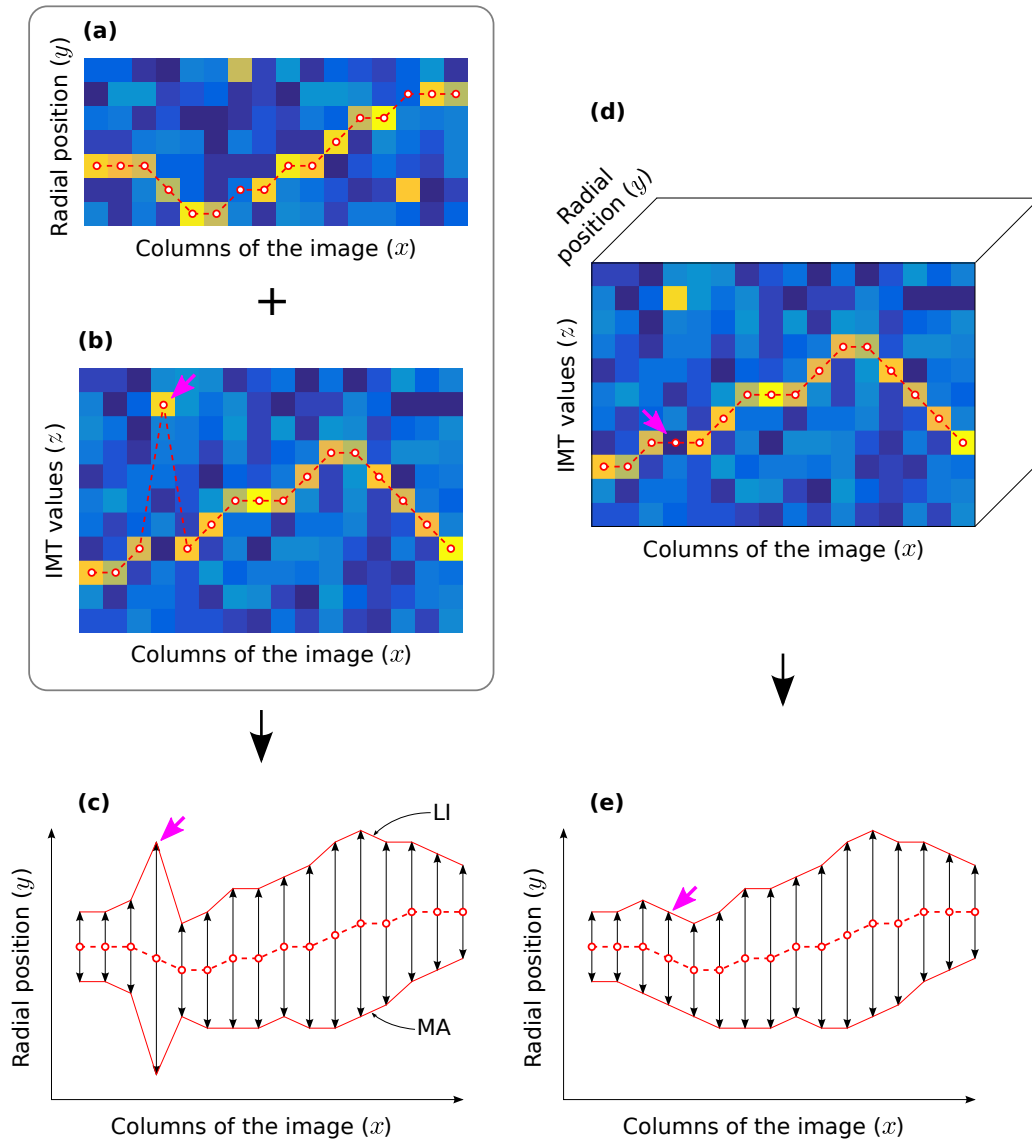


Figure 3: Schematic representation of the previously introduced segmentation method (left), compared with the approach proposed in the present study (right). The medial axis is represented by the red dashes, the two lumen-intima (LI) and media-adventitia (MA) contours are indicated by the red lines, and the Δ value (IMT) of each column in the image is displayed with the black arrows. In the previous method, a pair of 2D maps was used: a minimal path was extracted in a 2D space to describe the optimal radial position of the medial axis (a), and the Δ information was simply determined by selecting the maximum of a filter output (b), which may lead to erroneous results (c, pink arrow). In the present method, the minimal path is extracted in a 3D space (d) to describe the optimal medial axis (e). Please note that the spatial dimension y of the path is not fully represented in (d).

198 *Contour extraction*

199 In the new proposed method, all the K functions F_{Δ^k} are concatenated to build a
 200 single 3D velocity function F (Fig. 2c). More precisely, each map F_{Δ^k} is first down-
 201 sampled by a factor 10 in the radial direction, back to the original image resolution,
 202 in order to reduce the computational time as compared to down-sampling at a later
 203 stage of the work-flow. Subsequently, a 3D cost function \mathcal{C} , where the lowest values
 204 (blue color in Figure 2d) correspond to the points most likely to belong to the medial
 205 axis, is generated according to Equation 4.

206 *Dynamic programming.* Using the 3D cost function \mathcal{C} , a front propagation scheme
 207 is run to build a 3D cumulative cost function \mathbb{C} (Fig. 2e). Within the 3D space,
 208 the following x, y, z notation was adopted: x and y correspond to the horizontal and
 209 vertical coordinates in the 2D US image, respectively, and z represents the additional
 210 dimension corresponding to Δ , *i.e.*, tentative IMT values.

211 The propagation is unidirectional along x (*i.e.*, from the left to the right border of
 212 the sub-image \mathcal{I}_T), and favors the valleys in \mathcal{C} while penalizing abrupt changes along y
 213 and z , corresponding to non-horizontal contours and IMT variations, respectively.
 214 The values of \mathbb{C} where $x = 1$ (*i.e.*, the leftmost column of the ROI) are initialized
 215 with the corresponding values of \mathcal{C} . Then, the function \mathbb{C} is iteratively generated for
 216 increasing values of x , with x ranging from 2 (*i.e.*, second leftmost column of the
 217 ROI) to W (*i.e.*, rightmost column of the ROI), according to Equation 5.

$$\begin{aligned} \mathbb{C}(x, y, z) = \min_{d_y, d_z} \left\{ \mathbb{C}(x-1, y+d_y, z+d_z) \right. \\ \left. + \left(\mathcal{C}(x, y, z) + \mathcal{C}(x-1, y+d_y, z+d_z) \right) \cdot \left((1 + \alpha_y \cdot d_y^2) + (1 + \alpha_z \cdot d_z^2) \right) \right\} \end{aligned} \quad (5)$$

218 Here, $d_y \in \{-N_y, \dots, 0, \dots, N_y\}$ and $d_z \in \{-N_z, \dots, 0, \dots, N_z\}$ respectively represent
 219 displacements along the axes y and z , so the respective numbers of reachable neigh-
 220 bors along these directions are $2N_y + 1$ and $2N_z + 1$. The parameters α_y and α_z
 221 control the smoothness of the medial axis along y and z directions, respectively. Let
 222 us also note that the propagation function (Eq. 5) is symmetrical along the x di-
 223 rection, namely it yields identical results for left-to-right or right-to-left propagation
 224 schemes.

225 Finally, the point on the right border of \mathcal{I}_T with the minimal cumulative cost is
 226 found, and the minimum-cost path, P , corresponding to the global optimal solution,
 227 is extracted by back-tracking the decreasing values in \mathbb{C} from this identified point to
 228 the left border (Fig. 2f). By construction, for each value of x , there is a single point
 229 in P , so it can be written as $P \equiv \{(x, y, z) : x \in [1, W], y = P_y(x), z = P_z(x)\}$.

230 *Inverse transformation T^{-1} .* For each column x of the image, y and z coordinates
 231 of the minimum-cost path respectively indicate the radial position, $P_y(x)$, of the
 232 corresponding medial-axis node in the transformed image \mathcal{I}_T and the local IMT,
 233 $P_z(x)$. The final medial axis position is determined by mapping back the positions
 234 $P_y(x)$ onto the original image \mathcal{I} by the T^{-1} operation. Let $y_p(x)$ stand for the
 235 position $P_y(x)$ transformed by the T^{-1} operation. For each column x of the image,
 236 the coordinates of the two contours $y^-(x)$ (LI interface) and $y^+(x)$ (MA interface) of
 237 the intima-media complex are then deduced from the final medial axis (Fig. 2g and
 238 Fig. 3 right), according to the relation

$$y^\pm(x) = y_p(x) \pm 0.5 * P_z(x). \quad (6)$$

239 Finally, the global IMT of the image is calculated as the median radial distance
 240 between the LI and MA interfaces over the width W .

241 *Automatic initialization*

242 Prior to processing a given frame $\mathcal{I}(n)$, three parameters are required to run the
 243 method: *i)* the left and right boundaries of the ROI, \mathcal{I}_W , to be segmented, *ii)* the
 244 approximate location and shape of the far wall, and *iii)* the approximate IMT. When
 245 processing the n^{th} frame of a cine-loop, this input is obtained from the segmentation
 246 results of the previous $n - 1^{\text{st}}$ frame. For the first frame of the cine-loop, or a static
 247 image, these parameters must be provided by the initialization phase. In this work,
 248 the initialization is fully automatic, *i.e.*, no user interaction is required, whereas it
 249 was manual in our previous work. This automatic process is composed of three main
 250 steps described in the following paragraphs.

251 *Border clipping.* First, the outer top, bottom, left and right borders of the image
 252 that contain various text information such as the date and the scanner settings
 253 are removed to keep only the central region corresponding to the image of the vessel
 254 (Fig. 4a). For every pixel of the image, a score is computed by calculating the average
 255 absolute difference of gray level between every pair of consecutive images in the
 256 cine-loop. Outer borders correspond to low-score regions since pixels remain quasi-
 257 identical through the entire cine-loop, whereas the central vessel image corresponds
 258 to high-score regions since pixels are constantly changing between different frames.
 259 The image is thus clipped by applying a threshold τ on the horizontal and vertical
 260 profiles of the calculated scores.

261 *Localization of the far wall.* Second, an approximate location of the far wall is deter-
 262 mined by finding the regions with the strongest positive vertical gradient. To avoid

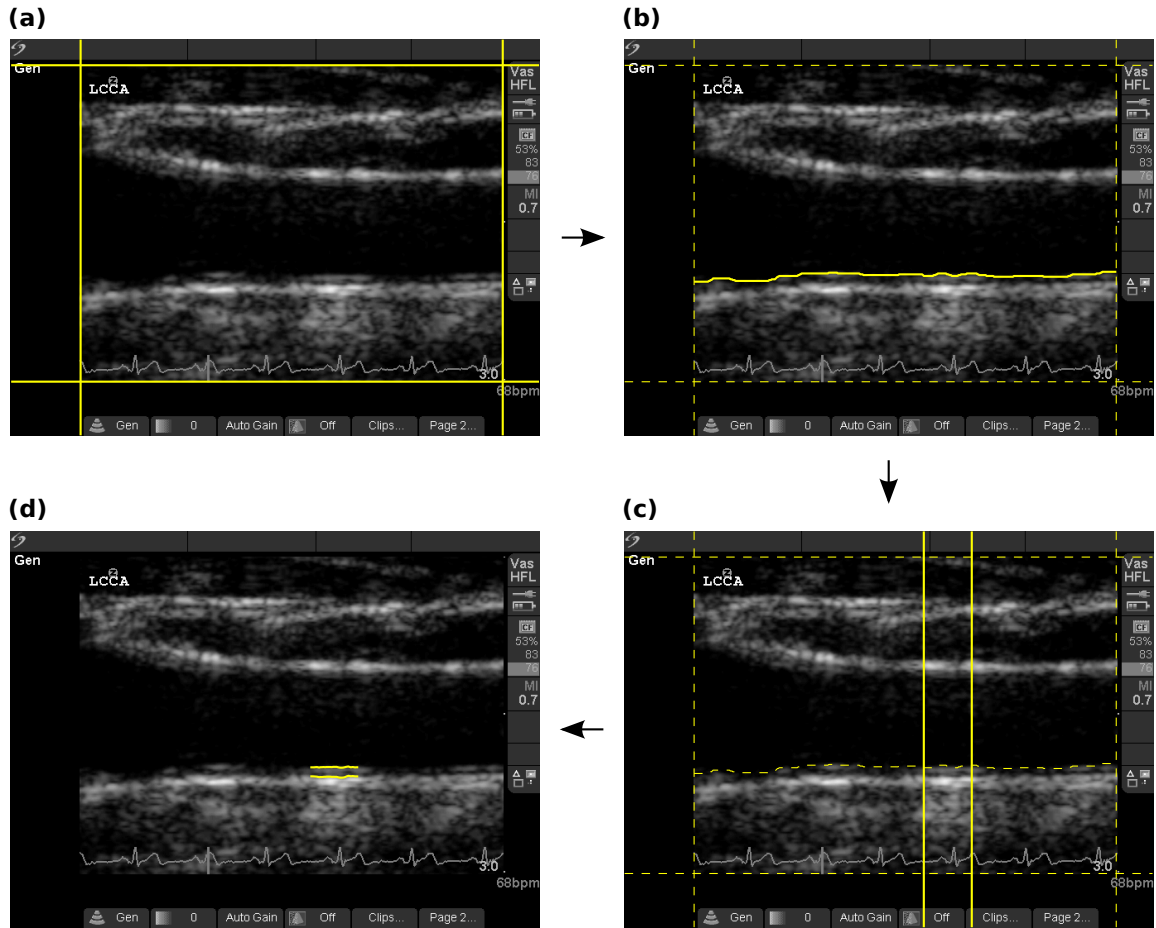


Figure 4: Illustration of the 4 stages of the fully-automatic process. (a) Border clipping. (b) Localization of the far wall. (c) Determination of the optimal region. (d) Contour segmentation.

263 potential errors that could be caused by the presence of the jugular vein, which ex-
 264 hibits a similar structure and is located (in the image) above the carotid artery, the
 265 search is only conducted in the bottom of the image, up to $h\%$ of the total image
 266 height. A heavily blurred vertical intensity gradient is calculated by column-wise
 267 convolution with a filter G'_B , defined as the first derivative of a Gaussian with a large
 268 standard deviation B . It is then used to build a cost function where lower costs
 269 correspond to larger positive gradients. A single contour is subsequently extracted
 270 (Fig. 4b) by a classical 2D minimum-cost-path search with this cost function, imple-

271 mented in a dynamic-programming scheme. The resulting rough contour of the far
272 wall constrains the search of the initial medial axis in the last step of the initialization.

273 *Determination of the optimal region and of the initial IMT.* Since some regions of
274 the far wall are frequently too noisy and not sufficiently contrasted to be segmented
275 accurately, a ROI, \mathcal{I}_W , with the best image quality, is localized. From our experi-
276 ence, its width $W = 3$ mm provides the optimal results to extract a reproducible
277 compression-decompression pattern (Zahnd et al., 2013b); a region too narrow of-
278 ten yields noisy curves of IMT temporal variation, and a region too broad generally
279 yields blurred curves. To find this optimal region, the contour segmentation method
280 introduced in this study is tentatively applied to the entire width of the image. Let
281 us recall however, that – at this stage – only an approximate location and shape of
282 the far wall are available, but IMT is not. Estimating the initial IMT, localizing
283 the optimal ROI, as well as refining the initial location of the line supposed to fall
284 mid-way between the two contours, are jointly performed in this last step of the
285 initialization process. The previously extracted location of the far wall is used to
286 apply the “flattening” transformation T . A set of K tentative IMT values, linearly
287 distributed in a large range between 0.4 mm and 1.5 mm, are assessed. Then, a score
288 is calculated for every column of the image, by extracting the output value of the
289 velocity function F_Δ (Eq. 2) at the location of the medial axis resulting from the
290 segmentation. Here, regions with good image quality are expected to have a high
291 score since they present well perceptible lumen-intima and media-adventitia inter-
292 faces. The optimal region \mathcal{I}_W is thus selected by finding the 3 mm segment with
293 the highest total score (Fig. 4c). Finally, the initial IMT is selected like in the main
294 method, by selecting the median radial distance between the contours resulting from
295 this tentative segmentation, within \mathcal{I}_W . The results of this step, *i.e.*, the borders of
296 \mathcal{I}_W , the approximate IMT, and the spatial location of the medial axis resulting from
297 the tentative segmentation, are passed as input parameters to the actual contour
298 segmentation applied within \mathcal{I}_W (Fig. 4d).

299 Experiments

300 *Study population*

301 All subjects were retrospectively selected from already acquired data used in
302 previous studies. Subjects presenting an atheromatous plaque in the imaged region,
303 as visually assessed by a medical doctor, were excluded from our study. A total of 244
304 subjects were included in the present study. To assess the accuracy and robustness
305 of the proposed method on data with various image characteristics and quality, the
306 present study involved a total of six cohorts from four different research centers, as
307 presented in Table 1. Representative examples of images from the six different cohorts
308 are displayed in Figure 5. The image data collection was conducted in compliance
309 with the requirements of the Institutional Review Boards in the different research
310 centers. Informed written consent was obtained from all subjects. The characteristics
311 of the cohorts involved are described hereafter.

312 *Erasmus MC, The Netherlands.* The first 51 subjects included in the PARISK study
313 (Truijman et al., 2014) at the Erasmus Medical Center, the Netherlands, were consid-
314 ered. The subjects were individuals with high cardiovascular risk; the main inclusion
315 criteria were a transient ischemic attack or a minor stroke in the past six weeks be-
316 fore enrollment, and a stenosis $< 70\%$ in the carotid bifurcation. Eight subjects were
317 rejected from the study, because they had an atherosclerotic plaque in the imaged
318 region. The remaining 43 subjects (denoted NLd) were included in the study.

319 *University of Lyon, France.* Fifty-seven healthy controls (FRc) and 25 patients
320 (FRd) at high cardiovascular risk were involved. Data acquisition was performed at
321 Louis Pradel Hospital (Lyon, France), as previously described (Zahnd et al., 2013a).
322 The inclusion criterion for the at-risk patients was the presence of one of the following
323 diseases diagnosed at least 1 year before: metabolic syndrome, or type 1 or 2 dia-
324 betes. No other criterion, including clinical characteristics, was used to select these
325 subjects. Healthy controls were cardiovascular-risk-factor free (tobacco use, hyper-
326 cholesterolemia, diabetes, hypertension, or particular family history), as assessed by
327 an oral questionnaire.

328 *Sydney Medical School, Australia.* Thirty healthy controls (AUc) and 30 patients
329 (AUd) were selected from the database of the PerioCardio study (Kapellas et al.,
330 2014). The images were collected at the Menzies School of Health Research in Dar-
331 win, Northern Territory, Australia. The at-risk patients were Aboriginal Australian
332 with moderate periodontitis, an emerging cardiovascular risk factor (Bouchard et al.,
333 2010). The healthy controls were age-matched Caucasian subjects without cardio-
334 vascular risk factors.

335 *University of Cyprus, Cyprus.* Data were gathered by downloading a publicly-available
 336 dataset containing 100 images recorded at the Cyprus Institute of Neurology and Ge-
 337 netics (Nicosia, Cyprus) (Loizou et al., 2007). All subjects were at risk of atheroscle-
 338 rosis and had already developed clinical symptoms, such as stroke or transient is-
 339 chemic attack. Forty-one patients were imaged twice, and the corresponding 41
 340 images were rejected to keep a single image per patient. The remaining 59 images
 341 (CYd) were included in the study.

Table 1: Characteristics of the six cohorts involved in the present study. (* The 100 initial images of the dataset from the University of Cyprus correspond to 58 males and 42 females with a mean age of 54 y.o. Nevertheless, 41 of these subjects were imaged twice. Therefore, the actual sex and age information for the 59 subjects of the CYd cohort is unknown.)

Medical center	Cohort name	Diseased/Control	n	Training set	Testing set	Gender (males)	Mean Age (years)
Erasmus MC, The Netherlands	NLd	Diseased	43	13	30	36	69.1 ± 7.5
University of Lyon, France	FRc	Control	57	19	38	24	37.9 ± 14.1
University of Lyon, France	FRd	Diseased	25	8	17	16	56.2 ± 10.5
Sydney Medical School, Australia	AUc	Control	30	0	30	17	41.0 ± 16.4
Sydney Medical School, Australia	AUd	Diseased	30	0	30	22	40.3 ± 8.9
University of Cyprus, Cyprus	CYd	Diseased	59	20	39	*	*

342 *Acquisition of carotid artery ultrasound images*

343 Longitudinal B-mode US images of the CCA were acquired for all subjects. The
 344 subjects were examined in the supine position. Image acquisition was performed
 345 with a clinical scanner equipped with a linear array transducer. The characteristics
 346 of the specific scanner used for each cohort are described in Table 2. For all but one
 347 (CYd) cohort, images were recorded through at least two consecutive full cardiac
 348 cycles, whereas for the CYd cohort only a single static image was available for each
 349 patient. The average (\pm std) number of frames for each cine loop was 206 ± 145 (range
 350 [66 – 491]). All image data were digitally stored and transferred to a commercial
 351 computer for off-line image analysis.

352 *Generation of training and testing sets*

353 Each cohort was divided into a training set and a testing set. The training
 354 datasets were used during the development phase of the method, to empirically de-
 355 termine the optimal parameter settings. The testing datasets were used only during
 356 the evaluation phase of the method, to determine the performance of the developed
 357 framework on independent test data. The distribution of the training and testing
 358 sets for each cohort is detailed in Table 1.

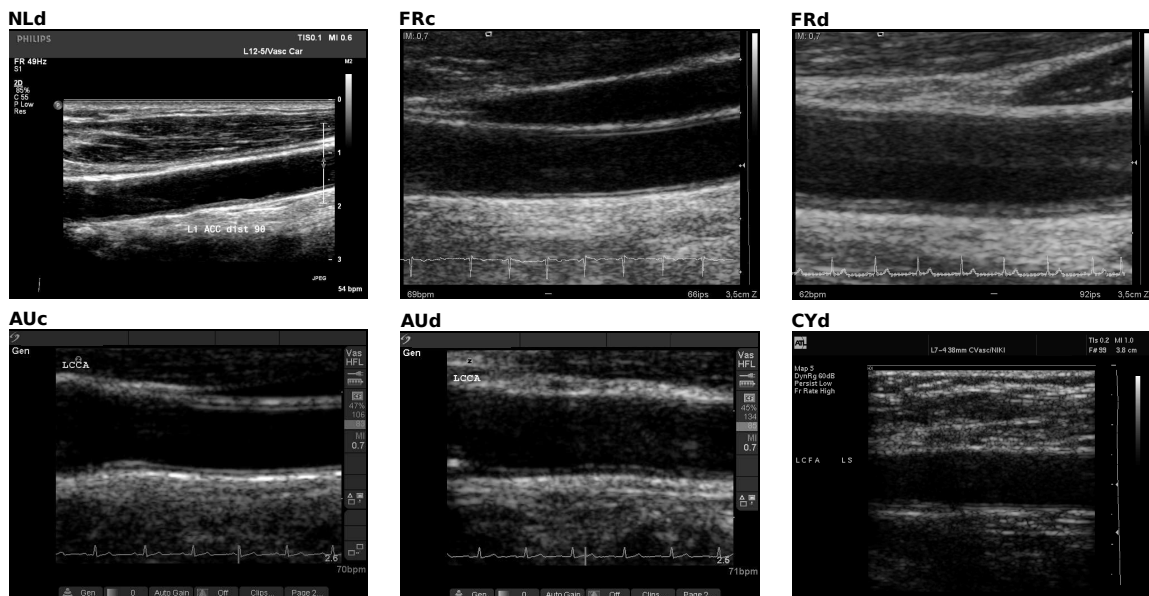


Figure 5: Representative images from the six different cohorts.

Table 2: Characteristics of the different ultrasound scanners used for the six cohorts.

Cohort name	Scanner	Transducer (MHz)	Pixel size (μm)	Frame-rate (fps)
Nld	iU22, Philips Medical Systems Bothell, USA	5–17 or 5–12	94 ± 9	40
FRc, FRd	Antares, Siemens Erlangen, Germany	7.5–10	34 ± 5	26
AUc, AUd	Sonosite MicroMaxx WA, USA	5–10	52 ± 4	24
CYd	HDI-3000, Advanced Technology Laboratories, Seattle, USA	4–7	67 ± 0	–

359 For all but two (AUc and AUd) cohorts, the training set was generated by ran-
 360 domly selecting a sub-sample of subjects (*i.e.*, roughly one third of the total number
 361 of subjects), and the testing set was generated with all the remaining subjects. For
 362 both AUc and AUd cohorts, the training datasets are empty. The reason for this
 363 decision was to evaluate the method on images with new unknown characteristics, by
 364 directly applying the proposed framework on the full AUc and AUd datasets without
 365 any prior training on images from these two specific cohorts.

366 *Independent standard*

367 To quantify the accuracy of the method, despite the lack of ground truth inherent
 368 to *in vivo* imaging, reference contours were traced by an experienced analyst \mathcal{A}_1 , on

369 the entire exploitable width of one image per subject. For the Nld, FRc, FRd,
 370 AUc and AUd cohorts, the first frame of the cine-loop was selected. First, as the
 371 left and/or right borders of the image sometimes show blur, low echoes, or high
 372 noise, the analyst \mathcal{A}_1 was asked to clip out the poor-quality borders, if necessary,
 373 thus defining the ROI to be considered. Subsequently, the analyst \mathcal{A}_1 performed
 374 the manual segmentation of both LI and MA interfaces, using a graphical interface
 375 that was developed in house specifically for this purpose. Continuous contours were
 376 generated by fitting a curve through a collection of carefully placed control points.
 377 The curve interpolation was done by means of the MATLAB *pchip* function. Two
 378 other analysts, \mathcal{A}_2 and \mathcal{A}_3 , who were blinded to the other results, manually traced the
 379 anatomical interfaces LI and MA, within the same ROIs of the same set of images.
 380 These tracings were used to assess inter-operator variability. Similarly, to assess
 381 intra-operator variability, \mathcal{A}_1 performed one week later a second manual delineation
 382 of the contours¹.

383 *Parameter settings and implementation*

384 The optimal parameter settings were empirically determined using the training
 385 set ($n = 60$), then the method was applied once to all the images of the testing set
 386 ($n = 184$) using the following configuration: height of the region centered around
 387 the medial axis used in the transformation T , $H = 3$ mm; minimal and maximal
 388 IMT threshold values, $\Delta_{\text{MIN}} = 0.4$ mm and $\Delta_{\text{MAX}} = 1.5$ mm, respectively; standard
 389 deviation of the Gaussian functions G_{σ_x} and G_{σ_y} , $\sigma_x = 150$ μm and $\sigma_y = 100$ μm ,
 390 respectively; smoothness parameters, $\alpha_y = 2$ and $\alpha_z = 0.1$; number of reachable
 391 neighbors along the y and z dimensions, $2N_y + 1 = 5$ and $2N_z + 1 = 5$. The number K
 392 of possible values Δ^k of the IMT depends of the spatial resolution of the image: the
 393 range between Δ^{min} and Δ^{max} was equal to 1 mm, with an increment δ between
 394 the K slices equal to 0.1 pixel (for example, $K = 200$ for an image with a spatial
 395 resolution of 50 μm). Setting δ in pixels² was motivated by the consistency between
 396 the three dimensions of the search space: with a finer image resolution one can expect
 397 a finer estimate of the IMT. The standard deviation B of the Gaussian function G_B
 398 was equal to 1 mm. In the automatic initialization process, the parameter τ used
 399 in border clipping, was equal to 3% of the highest score calculated in the given cine

¹For the CYp cohort, reference tracings were collected together with the images of the publicly-available dataset (Loizou et al., 2007). For this specific cohort, the reference annotations were already performed by two different analysts. Tracings from a third analyst and intra-analyst variability were not available.

²Setting δ in millimeters would yield a constant value of K and a constant “slice thickness” of the 3rd dimension in the search space.

400 loop, whereas the height, h , limiting the search of the far wall in the bottom of the
401 image was set to 60% of the clipped-image height.

402 The algorithm was implemented in a graphical user interface (GUI), both devel-
403 oped in MATLAB (MATLAB 7.14, The MathWorks Inc., Natick, MA, USA, 2011).
404 A compiled executable version, along with a user guide, were made publicly avail-
405 able: <https://www.creatis.insa-lyon.fr/carolab/>. The GUI also includes an
406 optional interactive initialization enabling the user to manually define the inputs of
407 the algorithm, like in our previous work: (i) select a sub-image \mathcal{I}_W by clipping out,
408 if necessary, the left and/or right borders of the image beyond which the wall cannot
409 be clearly perceived due to poor image quality, (ii) indicate the approximate location
410 and shape of the far wall by positioning three points within the intima-media com-
411 plex, and (iii) provide a rough initial estimate of the IMT by positioning two radially
412 aligned points on the LI and MA interfaces. Although the focus of this work is the
413 fully automatic method, the manual initialization was also used in the evaluation, to
414 assess different steps of the whole process, as described in the next subsections.

415 *Evaluation of the segmentation accuracy*

416 To assess the accuracy of the proposed method, two distinct experiments were
417 carried out: with the fully-automatic procedure, and with the manual initialization
418 procedure described in the previous subsection. Both were performed for all images
419 annotated by \mathcal{A}_1 , \mathcal{A}_2 , and \mathcal{A}_3 in the testing set. The resulting contours and IMT
420 were compared to those corresponding to the manual annotations by \mathcal{A}_1 . For both LI
421 and MA interfaces, the unitary segmentation error $\epsilon(x)$ was defined as the absolute
422 distance between the reference contour manually traced by \mathcal{A}_1 and the estimated
423 contour, in the column x of the image. For each image, the IMT estimation error
424 was defined as the difference between the IMT estimated by the method and the
425 reference IMT value derived from \mathcal{A}_1 's annotations. The latter was calculated as the
426 median column-wise distance between the LI and MA reference contours traced by
427 \mathcal{A}_1 , over the width of the ROI used in the given experiment, *i.e.*, $W = 3$ mm in the
428 first experiment, and whole exploitable width defined by \mathcal{A}_1 , in the second one.

429

430 *Fully automatic process.* The aim of the first experiment was to assess the robustness
431 of each step in the fully-automatic initialization process (Fig. 4), as well as the accu-
432 racy of the segmentation method initialized by this process. The analyst \mathcal{A}_1 labeled
433 the result of each step either as a success or as a failure. During the evaluation,
434 failures were reported and corrected in a cascade, *i.e.*, failures at the k^{th} step were
435 manually corrected prior to conducting the $k + 1^{\text{st}}$ step, as described below.

- 436 • For the first step, success was defined as clipping out the entire top, bottom, left
437 and right borders of the frame, while conserving the full image of the artery
438 (Fig. 4a). Failures were corrected by the user manually indicating the real
439 borders (1 mouse click per erroneous border).
- 440 • For the second step, success was defined as getting a contour that remained
441 close to the far wall over the full width of the image (Fig. 4b). Failures were
442 corrected by the user manually tracing the approximate location and curvature
443 of the far wall (3 mouse clicks).
- 444 • For the third step, success was defined as a ROI of width $W = 3$ mm located in
445 a region with good image quality, where both LI and MA contours were clearly
446 visible (Fig. 4c). Failures were corrected by the user manually indicating the
447 center of the new ROI on the region with optimal image quality (1 mouse click).
- 448 • For the fourth step, success was defined as a correct segmentation of both LI
449 and MA interfaces (Fig. 4d). Failures were corrected by the user manually in-
450 dicated the IMT (2 mouse clicks) before re-running the segmentation method.

451 Let us note that the images of the cohort CYP are static frames, therefore the
452 first step could not be applied, because a cine-loop is required. Hence, this step was
453 not evaluated for that cohort, and the borders were manually indicated by \mathcal{A}_1 .

454 *Segmentation with interactive initialization.* The aim of the second experiment was
455 to assess the ability of the method to accurately extract the LI and MA interfaces in
456 the whole exploitable width, W , determined by the user, and to compare the results
457 with our previous work (Zahnd et al., 2013b). The initialization was performed by
458 the analyst \mathcal{A}_1 who defined the ROI \mathcal{I}_W , indicated the approximate location and
459 shape of the wall, and roughly determined the IMT. The same initialization was
460 used to run the proposed segmentation method and the previous one. To investigate
461 the impact of the manual initialization phase, the reproducibility of the segmentation
462 algorithm was also assessed. The method was thus applied twice on each image, with
463 the analyst \mathcal{A}_1 performing the initialization phase a second time – one week later –
464 within the same clipped \mathcal{I}_W region.

465 *Evaluation of the temporal variation of the IMT during the cardiac cycle*

466 The intima-media complex has been demonstrated to undergo a reproducible
467 compression-decompression pattern during the cardiac cycle (Selzer et al., 2001),
468 namely the IMT is maximal at the end of diastole and minimal during systole. The
469 amplitude of the IMT compression, denoted Δ_{IMT} and corresponding to the difference

470 between the diastolic and systolic values of the IMT, has been shown to be positively
471 correlated with cardiovascular risk factors (Boutouyrie et al., 2001; Meinders et al.,
472 2003; Polak et al., 2012b,a; Zahnd et al., 2013b).

473 To investigate this phenomenon, the proposed segmentation method was applied
474 to all subjects from both the training and testing datasets, except those from the
475 CYP cohort, as only one static image was available instead of a temporal cine-loop.
476 The fully-automatic initialization scheme was used to determine a region of width
477 $W = 3$ mm located in the far wall, and the IMT was then assessed in all frames of the
478 cine-loop with the contour segmentation method. For all the 185 analyzed subjects,
479 the amplitude Δ_{IMT} of the temporal variation of the IMT was finally measured by
480 the analyst \mathcal{A}_1 on the resulting time-series by indicating the maximal (*i.e.*, during
481 the diastole) and minimal (*i.e.*, during the systole) IMT values.

482 *Statistical analysis*

483 The Mann-Whitney U test was used to compare the values of the end-diastole
484 IMT, as well as the total amplitude of the IMT variation Δ_{IMT} during the cardiac
485 cycle, between at-risk patients and healthy controls. The paired t-test was used to
486 compare the errors between the present method and the one previously developed
487 by our team (Zahnd et al., 2013b). The value $p < 0.05$ was considered to indicate a
488 statistically significant difference. The Pearson’s correlation coefficient R was used
489 to calculate the correlation between the reference tracings and the results from the
490 method, as well as between the end-diastolic IMT and the amplitude Δ_{IMT} . All
491 statistical analyzes were performed using MATLAB.

492 **Results**

493 *Fully-automatic process*

494 Segmentation with fully-automatic initialization was evaluated in the 184 images
 495 of the testing set. Qualitatively, the robustness of each step was assessed as follows: 2
 496 failures for the first step (border clipping), no failure for the second step (localization
 497 of the far wall), 7 failures for the third step (determination of the region with the
 498 best image quality), and 3 failures for the fourth step (contour extraction). Results
 499 from the quantitative evaluation of the contour accuracy are presented in Table 3.

Table 3: Segmentation absolute errors (mean \pm SD) in μm , between the fully-automatic segmentation method and the manual tracings from \mathcal{A}_1 , in the testing set. Manual correction of the fully-automatic process was performed for 12 images.

	All ($n = 184$)	NLd ($n = 30$)	FRc ($n = 38$)	FRd ($n = 17$)	AUc ($n = 30$)	AUd ($n = 30$)	CYd ($n = 39$)
Lumen-Intima	47 ± 70	49 ± 37	38 ± 35	29 ± 20	34 ± 30	36 ± 35	94 ± 144
Media-Adventitia	55 ± 68	74 ± 65	29 ± 26	34 ± 29	51 ± 42	52 ± 60	110 ± 116
IMT	66 ± 90	88 ± 68	35 ± 28	19 ± 14	39 ± 31	50 ± 50	130 ± 156

500 *Segmentation in the full exploitable width, with interactive initialization*

501 The proposed method was successfully applied to all the images, in both training
 502 and testing sets. Both LI and MA interfaces of the wall were delineated, and the
 503 corresponding IMT was extracted. Representative examples of resulting segmented
 504 contours for subjects from the six cohorts involved are displayed in Figure 6.

505 For all the 244 subjects involved, the average width W of the analyzed sub-image
 506 \mathcal{I}_W was 20 ± 8 mm (range 3 – 51 mm), which corresponded to an average ratio of
 507 60 ± 22 % (range 10 – 100 %) of the full image width.

508 For both training and testing sets, the mean absolute errors (\pm standard de-
 509 viation) of the segmentation process are displayed in Table 4. These results were
 510 calculated by aggregating all the corresponding unitary segmentation errors in a
 511 single vector, prior to generating the mean absolute error and standard deviation.

512 To further analyze the results, it is insightful to compare the error magnitude
 513 with the size of the analyzed tissues, namely, the IMT. The mean value (\pm standard
 514 deviation) of the reference IMT, in the first frame of all the subjects assessed, was
 515 688 ± 164 μm . The relative errors were calculated as the ratio between each absolute
 516 segmentation error $|\epsilon(x)|$ and the corresponding individual reference IMT. The mean
 517 value (\pm standard deviation) of the relative error was equal to 7.5 ± 10.3 % for the LI
 518 interface, 8.9 ± 9.2 % for the MA interface, and 7.6 ± 8.2 % for the estimated IMT.

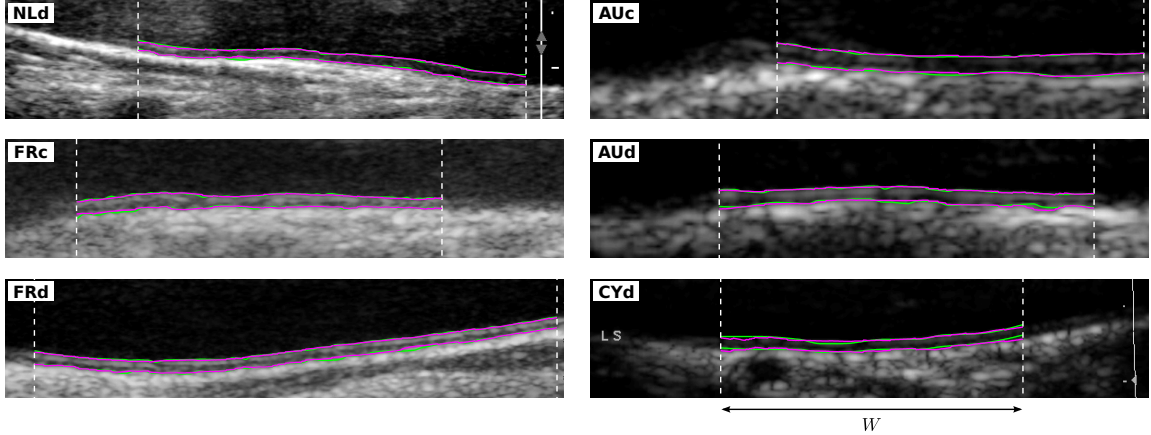


Figure 6: Results of the segmentation method (violet lines) compared to the reference contours traced by \mathcal{A}_1 (green lines), in subjects with varying image quality from the six cohorts involved. The left and/or right borders presenting poor image quality have been clipped out (vertical dashed lines) prior to segmenting the contours in the sub-image \mathcal{I}_W of width W .

519 The IMT estimated with the proposed method was in good correlation with
 520 reference tracings performed by \mathcal{A}_1 ($R = 0.87$), as depicted in Figure 7. The good
 521 agreement between the estimated IMT and the reference is also demonstrated in the
 522 Bland-Altman plot (Fig. 8), with a 95% confidence interval equal to $158 \mu\text{m}$ and a
 523 signed bias of $-11 \mu\text{m}$. The error introduced by the proposed method was very close
 524 to the inter- and intra-analyst variability, as displayed in Figure 9.

525 The computation time is proportional to the width of the investigated ROI and
 526 inversely proportional to the pixel size. On average, for a pixel size of $57 \mu\text{m}$ and a
 527 segment of width $W = 20 \text{ mm}$ (350 pixels), the processing time was 0.8 s per image.

528 The errors obtained with the previous method developed by our team (Zahnd
 529 et al., 2013b), are reported in Table 5. These results are to be compared with light-
 530 gray rows in Table 4. Comparing mean errors and standard deviations in the first
 531 column of these tables, it can be seen that the present method overall more accurately
 532 extracted LI and MA interfaces. More specifically, the mean absolute error for both
 533 LI and MA interfaces was smaller, with a near-statistically significant p -value of 0.08
 534 and 0.07, respectively. Although the mean absolute error resulting from the IMT
 535 estimation was slightly larger, the difference was not statistically significant ($p =$
 536 0.59). Moreover, contours resulting from the previous method had a much rougher
 537 aspect, since their smoothness was not explicitly controlled, as depicted in Figure 10.

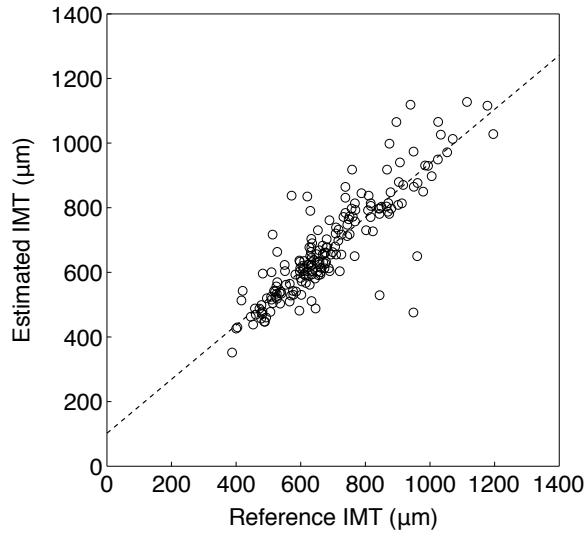


Figure 7: Linear regression line between the IMT estimated by the proposed method and the manual reference performed by \mathcal{A}_1 , for all 184 images of the testing set.

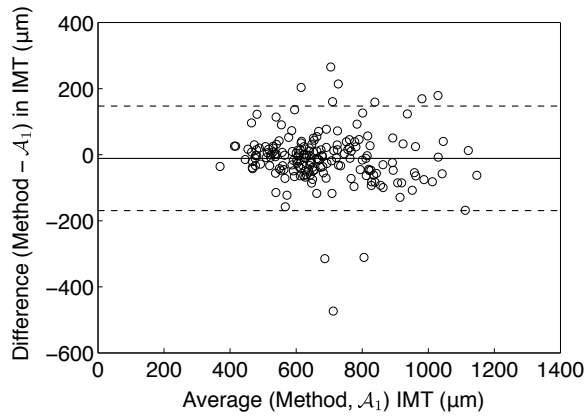


Figure 8: Bland-Altman plot, comparing the estimates of the IMT between the proposed method and the manual tracings performed by \mathcal{A}_1 , for all 184 images of the testing set. The solid and dashed lines represent the bias and the 95% limits of agreement, respectively.

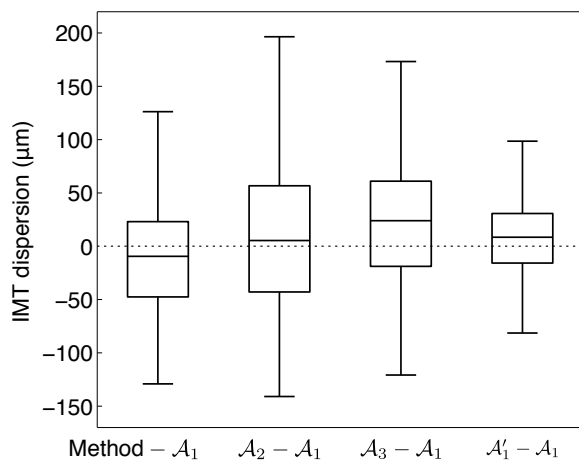


Figure 9: Box plot representing the dispersion between the IMT estimated with the proposed method and the manual tracings performed by \mathcal{A}_1 , compared to the inter- and intra-analyst variability, for all 184 images of the testing set. Percentiles are indicated by boxes (25th and 75th), inner lines (50th), and error bars (5th and 95th).

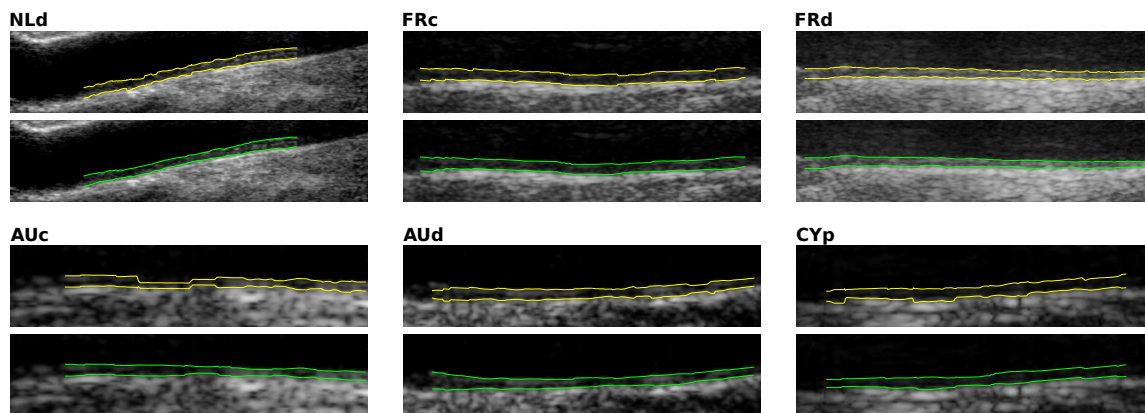


Figure 10: Example of segmented contours, for each cohort, resulting from the method previously proposed (Zahnd et al., 2013b) (yellow) and the present approach (green). The results show that the proposed method controls the smoothness of the contours.

Table 4: Segmentation absolute errors (mean \pm SD) in μm , for the proposed method with manual initialization and the manual tracings performed by the analysts $\mathcal{A}_{1,2,3}$.

Cohort	All ($n = 244$)	NLd ($n = 43$)	FRc ($n = 57$)	FRd ($n = 25$)	AUc ($n = 30$)	AUd ($n = 30$)	CYd ($n = 59$)
Training set	$n = 60$	$n = 13$	$n = 19$	$n = 8$	$n = 0$	$n = 0$	$n = 20$
Lumen-Intima							
Method vs \mathcal{A}_1	52 ± 73	64 ± 96	33 ± 27	32 ± 27	–	–	97 ± 110
Method reproducibility	27 ± 85	33 ± 28	11 ± 10	12 ± 10	–	–	67 ± 170
Inter-analysts	49 ± 53	76 ± 75	44 ± 42	31 ± 30	–	–	102 ± 70
Intra-analyst	31 ± 33	54 ± 50	28 ± 26	19 ± 16	–	–	–
Media-Adventitia							
Method vs \mathcal{A}_1	57 ± 61	66 ± 66	44 ± 51	37 ± 33	–	–	93 ± 76
Method reproducibility	30 ± 125	33 ± 36	11 ± 10	13 ± 11	–	–	77 ± 255
Inter-analysts	54 ± 60	102 ± 90	41 ± 42	43 ± 42	–	–	81 ± 65
Intra-analyst	35 ± 43	58 ± 49	30 ± 41	28 ± 33	–	–	–
IMT							
Method vs \mathcal{A}_1	67 ± 90	31 ± 24	28 ± 20	22 ± 24	–	–	144 ± 122
Method reproducibility	16 ± 73	5 ± 8	2 ± 3	4 ± 4	–	–	42 ± 125
Inter-analysts	57 ± 46	61 ± 46	51 ± 40	42 ± 30	–	–	149 ± 54
Intra-analyst	25 ± 24	31 ± 34	25 ± 18	17 ± 16	–	–	–
Testing set	$n = 184$	$n = 30$	$n = 38$	$n = 17$	$n = 30$	$n = 30$	$n = 39$
Lumen-Intima							
Method vs \mathcal{A}_1	49 ± 62	52 ± 59	39 ± 33	35 ± 38	36 ± 30	42 ± 41	92 ± 113
Method reproducibility	18 ± 28	28 ± 24	11 ± 15	11 ± 10	17 ± 15	17 ± 16	30 ± 55
Inter-analysts	56 ± 51	68 ± 60	47 ± 40	31 ± 29	70 ± 57	80 ± 52	85 ± 68
Intra-analyst	36 ± 36	50 ± 43	34 ± 36	26 ± 34	34 ± 28	37 ± 35	–
Media-Adventitia							
Method vs \mathcal{A}_1	59 ± 67	72 ± 60	43 ± 42	40 ± 42	52 ± 49	54 ± 61	104 ± 109
Method reproducibility	17 ± 26	31 ± 31	11 ± 10	12 ± 10	17 ± 18	14 ± 13	23 ± 49
Inter-analysts	69 ± 72	113 ± 95	40 ± 38	39 ± 40	100 ± 78	89 ± 79	92 ± 72
Intra-analyst	45 ± 50	65 ± 55	33 ± 40	34 ± 46	53 ± 48	59 ± 63	–
IMT							
Method vs \mathcal{A}_1	67 ± 67	52 ± 44	29 ± 21	36 ± 21	53 ± 31	62 ± 58	145 ± 87
Method reproducibility	5 ± 8	6 ± 10	2 ± 3	3 ± 5	6 ± 6	7 ± 10	7 ± 10
Inter-analysts	59 ± 52	87 ± 67	48 ± 36	35 ± 27	52 ± 51	58 ± 53	106 ± 28
Intra-analyst	34 ± 37	36 ± 26	31 ± 29	27 ± 28	31 ± 23	44 ± 64	–

Table 5: Segmentation absolute errors (mean \pm SD) in μm , between the previous method that was developed by our team (Zahnd et al., 2013b) and the manual tracings from \mathcal{A}_1 , in the full exploitable width of each image of the testing set.

	All ($n = 184$)	NLd ($n = 30$)	FRc ($n = 38$)	FRd ($n = 17$)	AUc ($n = 30$)	AUd ($n = 30$)	CYd ($n = 39$)
Lumen-Intima	55 ± 81	46 ± 53	37 ± 35	33 ± 34	56 ± 92	45 ± 51	119 ± 138
Media-Adventitia	68 ± 81	67 ± 69	42 ± 44	42 ± 37	71 ± 61	65 ± 73	138 ± 130
IMT	64 ± 75	45 ± 37	34 ± 30	28 ± 22	54 ± 47	59 ± 63	131 ± 109

538 *Temporal variation of the IMT during the cardiac cycle*

539 The temporal variation of the IMT was assessed in all available cine-loops, and
 540 a cyclic compression-decompression pattern could be observed during consecutive
 541 cardiac cycles, as displayed in Figure 11. For all subjects, the diastolic IMT was
 542 systematically greater than the systolic IMT, namely $766 \pm 174 \mu\text{m}$ *vs.* $670 \pm 163 \mu\text{m}$,
 543 respectively. The average amplitude Δ_{IMT} of the temporal variation of the IMT
 544 during the cardiac cycle was $97 \pm 43 \mu\text{m}$, and corresponded to $13 \pm 5\%$ of the end-
 545 diastole IMT.

546 Measurements from the diseased subjects (*i.e.*, NLd, FRd and AUd, $n=98$) were
 547 then compared to the healthy controls (*i.e.*, FRc and AUc, $n=87$), from both training
 548 and testing sets. The end-diastole IMT value, estimated with the fully-automatic
 549 segmentation method, was significantly higher in at-risk patients compared to healthy
 550 controls (855 ± 161 *vs.* $666 \pm 129 \mu\text{m}$, $p < 0.0001$). Furthermore, the amplitude
 551 Δ_{IMT} was also significantly higher in the diseased population compared to healthy
 552 volunteers (106 ± 48 *vs.* $86 \pm 34 \mu\text{m}$, $p = 0.001$), as shown in Figure 12. The
 553 end-diastole IMT value was not correlated with the amplitude Δ_{IMT} of the temporal
 554 variation of the IMT during the cardiac cycle ($R = 0.3837$).

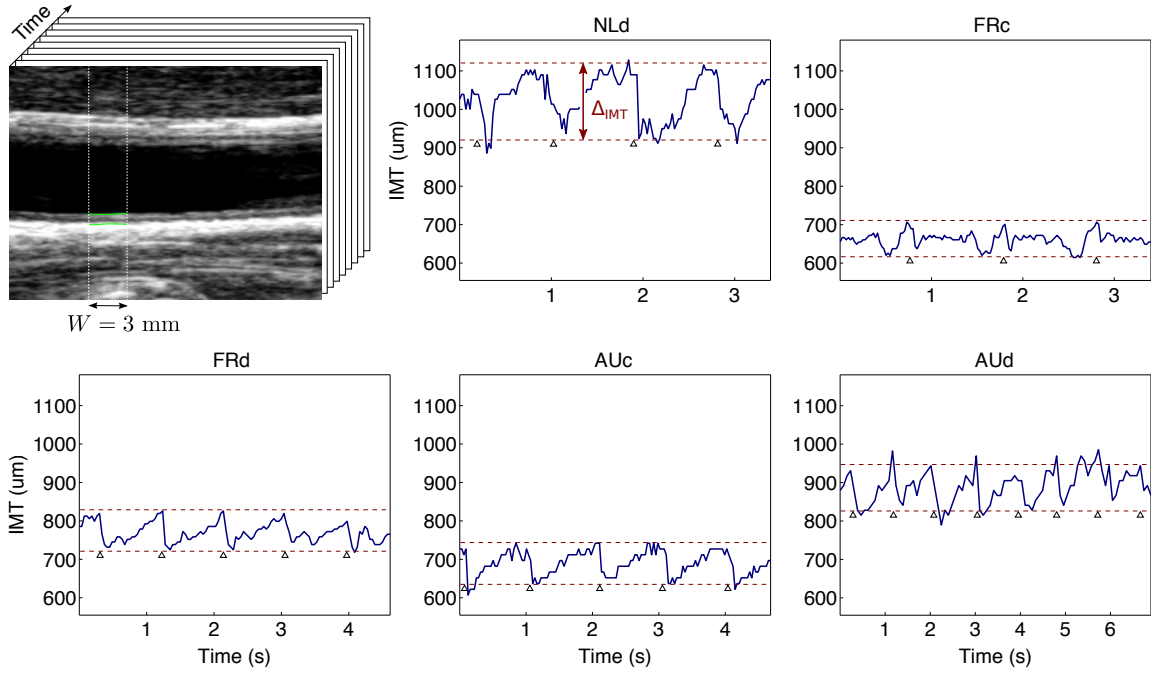


Figure 11: Temporal variations in IMT during several consecutive cardiac cycles. The IMT was quantified on a local region of reduced width ($W = 3$ mm) for all frames of the cine-loop (top left panel). Examples of the cyclic compression-decompression pattern of the IMT, resulting from the proposed fully-automatic method, are provided for subjects from different cohorts. The Δ_{IMT} parameter corresponds to the total amplitude of the IMT variations (dashed lines). The end of the diastole is indicated by the triangle markers.

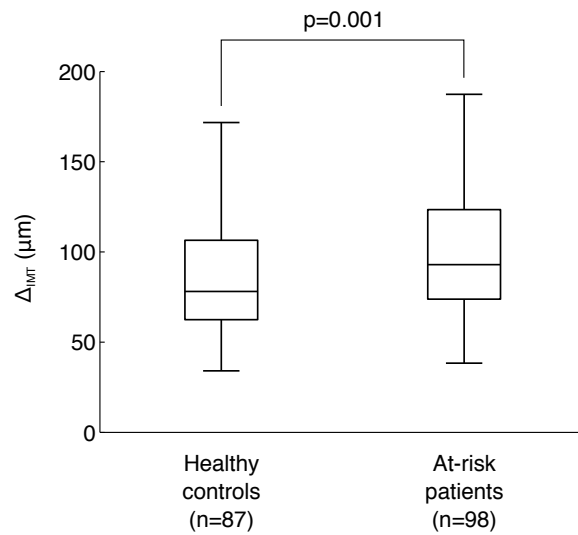


Figure 12: Box plot representing the amplitude Δ_{IMT} of the temporal variations in IMT during the cardiac cycle, for healthy controls and at-risk patients. Percentiles are indicated by boxes (25th and 75th), inner lines (50th) and error bars (5th and 95th). The result of the Mann-Whitney U test is indicated by the p value.

555 **Discussion**

556 The main contribution of this study is an original segmentation method devised
557 to simultaneously extract, from noisy images, both interfaces of thin structures with
558 nearly parallel contours. Although the method is fully-automatic, its implementation
559 allows quick interactive corrections, if necessary, at each step of the algorithm. It
560 was tuned to segment out the carotid artery intima-media complex in 2D US images.
561 These anatomical interfaces were successfully extracted for 244 subjects from six
562 different cohorts. The contours obtained and the calculated IMT values were close
563 to manual tracings from expert analysts, with spatial errors of the order of the pixel
564 size. The temporal variation of the IMT during the cardiac cycle was finally assessed
565 with use of the proposed method, and the amplitude of this variation was significantly
566 higher in at-risk patients compared to healthy controls, which is in accordance with
567 recent findings.

568 *Contour segmentation framework*

569 The method extracts a single medial axis, from which the contours of both LI
570 and MA interfaces can be fully deduced. Among all possible solutions, the globally
571 optimal medial axis is determined by means of a specific dynamic programming
572 scheme, in which a 3D cost function represents, for each column x of the image, all
573 potential radial positions, y , of the medial axis, as well as all potential IMT values, z .
574 Similar approaches have previously been introduced, to extract a globally optimal
575 $(n+1)$ -dimensional path that describes the n -dimensional contour of tubular objects,
576 with a front propagation technique based on a multi-scale filter (Wink et al., 2004),
577 as well as with fast-marching methods exploiting spheres of varying radius (Li and
578 Yezzi, 2007; Benmansour and Cohen, 2011).

579 The front propagation scheme (Eq. 5) favors solutions that are located mid-way
580 between two strong positive gradients (namely, LI and MA interfaces), while penaliz-
581 ing contours with irregular shapes. More precisely, the smoothness of the medial axis
582 is ruled by two penalty terms: the first one penalizing abrupt variations of the radial
583 position of the medial axis between adjacent columns, and the second one penalizing
584 sudden IMT variation, which would result in spiky contours even with a perfectly
585 smooth medial axis. In the case of a cine-loop, the medial axis from the previous
586 image is exploited as *a priori* information to characterize a spatial transformation T ,
587 used to encourage solutions presenting a similar shape and curvature. In the case of
588 a single image, a similar process is used by exploiting the information derived from
589 the initialization phase. The resulting output corresponds to a pair of continuous
590 and smooth contours that still capture the subtle spatial variation of the IMT within
591 a given image (Fig. 6).

592 The process is fully-automatic and does not require any user interaction. Nev-
593 ertheless, manual specification of part (or all) of the initialization settings can still
594 be performed by the operator in a quick and simple way *via* a convenient graphical
595 interface. Such manual corrections are sometimes necessary to increase the overall ro-
596 bustness of the method by avoiding errors that can be caused by the fully-automatic
597 process in some challenging cases. Manual initialization also enables the user to per-
598 form a case-by-case analysis by specifying the center of the desired ROI as well as
599 its width for each subject.

600 *Method evaluation*

601 The contour extraction method was applied in a set of 244 *in vivo* images gath-
602 ered from six different cohorts and four different research centers. Quite a large
603 discrepancy could be observed between the different cohorts in terms of image char-
604 acteristics and quality: FRc and FRd had a high image quality with generally well
605 visible anatomical interfaces, AUc and AUd had a medium image quality with more
606 blurry interfaces, NLd had an overall high image quality, but the interfaces were
607 not clearly detailed as the images were zoomed out, and CYd had a challenging
608 image quality with poorly visible interfaces. Image acquisition was performed with
609 a different scanner in each of the four medical centers, and a discrepancy was also
610 present in the spatial resolution of the images, with a pixel size equal to $94 \pm 9 \mu\text{m}$
611 for NLd, $34 \pm 5 \mu\text{m}$ for FRc and FRd, $52 \pm 4 \mu\text{m}$ for AUc and AUd, $67 \pm 0 \mu\text{m}$ for
612 CYd. Moreover, the discrepancy in image quality among the analyzed data was also
613 reflected by significantly varying width of the exploitable region, \mathcal{I}_W , as assessed by
614 observer \mathcal{A}_1 (range 10 – 100 % of the full image width).

615 The accuracy of the method, for both the fully-automatic and manual initial-
616 ization, was of the same order of magnitude as inter- and intra-analysts variability
617 (Tables 3, 4). Overall, the mean absolute error corresponded approximately to one
618 pixel. Variability of the method with the manual initialization process was sub-
619 stantially smaller than inter- and intra-analysts variability, which reflects a better
620 reproducibility. Variability of the method with the fully-automatic initialization
621 process was null (*i.e.* fully reproducible results), except when the automatic process
622 failed (*i.e.* 12 cases out of 184) and had to be manually corrected. Variability due to
623 such a manual correction was not assessed, but it is likely to be very close to vari-
624 ability of the manual initialization process for these specific cases (5% of the whole
625 population), but – averaged over the whole population – it is likely to be negligible.

626 The robustness of the method could also be verified, since images were separated
627 between a training set, used to determine the optimal parameters settings, and a
628 testing set, used to evaluate the method in independent test images. Let us first

629 note that the errors for the testing set were of the same magnitude as the errors
630 for the training set, which reflects a certain consistency in the performances of the
631 method. Moreover, when applying the method on the AUc and AUd datasets without
632 any prior training on these two cohorts, good results were also obtained. In view
633 of the above, the robustness of the method was demonstrated, since 244 images
634 were successfully segmented using the same parameter settings, despite differences
635 in arterial geometry, scanner configuration, and image quality.

636 A variety of methods have been introduced to segment the carotid artery in longi-
637 tudinal B-mode US images. When comparing the results of the present framework to
638 previous work reported in recent review articles (Molinari et al., 2010; Ilea et al., 2013;
639 Loizou, 2014), the present method would rank among the most accurate state-of-the-
640 art techniques. Nevertheless, such comparisons are to be taken carefully, since the
641 design of the evaluation protocol can greatly differ between distinct studies. Among
642 the most encountered differences are the nature of the cohorts involved (*e.g.*, number
643 of subjects and images, healthy volunteers and/or at-risk patients), the characteris-
644 tics of the images (*e.g.*, use of several different scanners, spatiotemporal resolution),
645 the distance metric (*e.g.*, mean absolute radial distance, or polyline distance), the
646 dimensions of the ROI (*e.g.*, full image width, limited region), the properties of the
647 initialization process (*e.g.*, fully-automatic or with manual input from the user), and
648 the characteristics of the manual reference annotations (*e.g.*, discrete control points
649 or continuous tracings, inter- and intra-analysts variability). To thoroughly estab-
650 lish a genuine comparison between multiple state-of-the-arts approaches, a challenge
651 would be necessary, where evaluation would be carried out homogeneously and in
652 the same datasets for all the methods.

653 *Temporal variation of the IMT*

654 The compression-decompression pattern of the arterial layers during the cardiac
655 cycle was analyzed by extracting the IMT in every frame of the cine-loop (Fig. 11).
656 This operation was performed in a ROI of reduced width $W = 3$ mm, located in a
657 well-contrasted region with clearly visible interfaces. From our experience, such a
658 narrow region with good image quality is better suited to extract the minute IMT
659 variations compared to the full width of the image (Zahnd et al., 2013b).

660 The IMT was significantly higher in at-risk patients compared to healthy controls
661 (855 ± 161 vs. 666 ± 129 μm , $p < 0.0001$), which reflects arterial wall thickening (Bal-
662 dassarre et al., 2000). Moreover, the diastolic IMT was systematically greater than
663 the systolic IMT for all subjects (766 ± 174 μm vs. 670 ± 163 μm), which is in
664 accordance with previous studies (Selzer et al., 2001; Meinders et al., 2003). The
665 amplitude Δ_{IMT} of the IMT variation during the cardiac cycle was also quantified,

666 and the average value for all subjects was $97 \pm 43 \mu\text{m}$. This is higher than the
667 results that were reported in previous studies that indicated a Δ_{IMT} value around
668 $50 \mu\text{m}$ (Boutouyrie et al., 2001; Meinders et al., 2003; Polak et al., 2012b,a). These
669 differences may be explained by the differences in the characteristics of the subjects
670 involved, contour segmentation methods, and measurement protocols.

671 Interestingly, Δ_{IMT} was significantly increased in at-risk patients compared to
672 healthy controls (106 ± 48 vs. $86 \pm 34 \mu\text{m}$, $p = 0.001$, Fig. 12); this result is
673 in agreement with recent findings showing that the amplitude of the compression-
674 decompression pattern of the arterial wall is associated with cardiovascular risk fac-
675 tors (Boutouyrie et al., 2001; Meinders et al., 2003; Polak et al., 2012a; Zahnd et al.,
676 2013b). More specifically, Δ_{IMT} has been demonstrated to be associated with pulse
677 pressure, LDL-cholesterol, and age (Polak et al., 2012b). Although it is beyond the
678 scope of the present study, these three factors might contribute to explain the overall
679 increase of the parameter Δ_{IMT} in the diseased population.

680 Each subject can thus be characterized by two different parameter values, namely
681 the diastolic IMT and the parameter Δ_{IMT} , as displayed in Figure 11. Although the
682 exact association of Δ_{IMT} with cardiovascular risk is still exploratory, this finding
683 can contribute to shed further light on potential early-stage symptoms of atheroscle-
684 rosis. IMT is a *static* parameter that marks the *presence* of atherosclerotic disease.
685 Nevertheless, it has recently been demonstrated to have limited additional predic-
686 tive power over conventional risk factors (Kavousi et al., 2012). On the other hand,
687 the amplitude Δ_{IMT} is a *dynamic* parameter that is likely to be directly related to
688 the *effect* of the disease on mechanical properties of the arterial wall, as well as the
689 functional role of arterial-wall cells. Furthermore, compression of the arterial wall is
690 a crucial physiological mechanism, as it enables fluid exchange between blood and
691 surrounding tissues (Chuong and Fung, 1984). Let us also recall that the end-diastole
692 IMT value was not correlated with Δ_{IMT} ($R = 0.3837$). For all these reasons, the
693 parameter Δ_{IMT} is likely not to replicate information already provided by static IMT
694 measurements, but may instead yield complementary information in cardiovascular
695 risk assessment. Such analysis was out of the scope of the present study.

696 When attempting to assess the temporal variation of the IMT in US cine-loops,
697 several recommendations should be considered. First, the spatial resolution of the
698 scanner plays a major role. The total amplitude of the compression phenomenon
699 is around $100 \mu\text{m}$, therefore a pixel size $> 100 \mu\text{m}$ is likely to yield inaccurate re-
700 sults, despite the tenfold interpolation used in the method. The accuracy of the
701 method is expected to increase when decreasing the pixel size. Although a finer spa-
702 tial resolution might result in an increment of the computational time, this may be
703 compensated by as smaller interpolation factor. Second, as the studied phenomenon

704 is dynamical, the temporal resolution (frame-rate) should be sufficient to capture
705 several images per cardiac cycle. From our experience, frame-rates > 15 fps are
706 generally sufficient to assess the compression amplitude, but higher values may be
707 necessary for subjects with particularly fast heartbeat and/or to study the shape of
708 the compression curves. It should however be noted that increasing the temporal
709 resolution generally results in decreasing the spatial resolution. Third, image acqui-
710 sition should be performed during at least one entire cardiac cycle to capture the full
711 compression-decompression pattern. Acquiring several cardiac cycles may be useful
712 to exploit the reproducibility of this pattern, but all the acquired frames must rep-
713 resent the same section of the arterial wall. Therefore, special care shall be taken to
714 maintain the transducer steady, while the patient refrains himself/herself from mov-
715 ing, swallowing, and – preferably – breathing. In practice, we recommend acquiring
716 three cardiac cycles, as a reasonable trade-off between reproducibility, and the risk
717 of undesired effects due to patient’s movements or unsteady transducer position.

718 *Limitations and perspectives*

719 The method is based on a 3D front propagation approach (namely, along the
720 radial, longitudinal, and IMT dimensions) to extract a pair of spatially smooth con-
721 tours from a 2D image. However the temporal dimension *per se* is not implemented
722 in the front propagation scheme (Eq. 5). When processing several consecutive images
723 in a cine-loop, the output from a given frame is used as a robust *a priori* information
724 to initialize the search in the following frame. Although the contours are accurately
725 extracted in each individual frame, the up-and-down motion of these contours be-
726 tween successive images is not regularized by a smoothing parameter. Accordingly,
727 taking into consideration the spatio-temporal consistency of the contours by extend-
728 ing a previously proposed surface-fitting approach (Metz et al., 2011) to a 3D+t
729 volume could potentially contribute to the improvement of the method.

730 According to the Mannheim expert consensus (Touboul et al., 2012), optimal
731 IMT measurements should be performed at least 5 mm from the carotid bifurcation.
732 In the proposed fully-automatic scheme, the selection of the assessed region is based
733 on image quality, and may therefore, in some cases, be closer than 5 mm from the
734 bulb. The expert consensus also recommends to carry out IMT measurements over
735 a section of 10 mm. In the present study, the IMT variation was evaluated on a
736 narrow region of 3 mm because, from our experience, this width provides the opti-
737 mal results to extract a reproducible compression-decompression pattern (Fig. 11).
738 Curves obtained from regions $\ll 3$ mm are often corrupted by noise because too few
739 local measurements are averaged to generate the IMT value and, conversely, curves
740 from regions $\gg 3$ mm are generally flat smooth lines without much variation due to

741 excessive averaging; in both cases the cycles cannot be clearly perceived, and the am-
742 plitude Δ_{IMT} cannot be reliably quantified. It is also noteworthy that the temporal
743 variation of the IMT is an emerging dynamical parameter and is not mentioned in
744 the consensus. Moreover, the full exploitable width of all the analyzed images ranged
745 from 3 to 51 mm, and therefore some cases could not have met the 10 mm required
746 by the consensus. Nevertheless, the user can easily and quickly select the center of a
747 more suited region (1 mouse click) and/or modify the width of the analyzed section
748 (2 mouse clicks), if necessary.

749 The purpose of the method is to extract both LI and MA interfaces of the ar-
750 terial wall in images of asymptomatic subjects to extract quantitative markers of
751 early-stage atherosclerosis, such as arterial wall thickening. The method might be
752 sub-optimal when applied to images presenting an atherosclerotic plaque, since the
753 rationale is to detect two nearly-parallel contours. A distinct set of parameters (*viz.*,
754 with smaller smoothness penalties and a larger tolerated thickness) could enable
755 processing of such images with a plaque – thus yielding a measurement of plaque
756 thickness and length, but potentially also (semi-) automatic plaque detection – yet
757 it is likely to hinder the performances of the method in asymptomatic regions.

758 *Conclusion*

759 A fully-automatic method based on front propagation was introduced to segment
760 the the intima-media complex in carotid B-mode ultrasound. A globally optimal 3D
761 path was extracted to describe a pair of 2D contours. The method was devised to
762 accurately extract the IMT in every column of the image. The performances of the
763 framework were validated in 184 independent test images. The proposed approach
764 was successfully applied to quantify the amplitude of the compression-decompression
765 pattern of the intima-media complex during the cardiac cycle, which may potentially
766 be a risk marker of early-stage atherosclerosis. The algorithm was implemented in a
767 graphical user interface and is available on-line: [https://www.creatis.insa-lyon.
768 fr/carolab/](https://www.creatis.insa-lyon.fr/carolab/).

769 **Acknowledgements**

770 The authors are grateful to Prof. Leonardo Flórez-Valencia for his valuable ad-
771 vices on the front propagation method, and to Mr. Antoine Courcelles for his useful
772 contributions to the front propagation method and the fully-automatic initialization
773 scheme. This work was partly supported by the LABEX ANR-11-LABX-0063 of
774 Université de Lyon, within the program “Investissements d’Avenir” (ANR-11-IDEX-
775 0007) operated by the French National Research Agency (ANR).

776 **References**

- 777 Baldassarre D, Amato M, Bondioli A, Sirtori CR, Tremoli E. Carotid artery intima-
778 media thickness measured by ultrasonography in normal clinical practice correlates
779 well with atherosclerosis risk factors. *Stroke*, 2000;31:2426–2430.
- 780 Bastida-Jumilla MC, Menchón-Lara RM, Morales-Sánchez J, Verdú-Monedero R,
781 Larrey-Ruiz J, Sancho-Gómez JL. Frequency-domain active contours solution to
782 evaluate intima–media thickness of the common carotid artery. *Biomedical Signal*
783 *Processing and Control*, 2015;16:68–79.
- 784 Benmansour F, Cohen LD. Tubular structure segmentation based on minimal path
785 method and anisotropic enhancement. *International Journal of Computer Vision*,
786 2011;92:192–210.
- 787 Bouchard P, Boutouyrie P, D’Aiuto F, Deanfield J, Deliargyris E, Fernandez-Avilés
788 F, Hughes F, Madianos P, Renvert S, Sanz M. European workshop in periodontal
789 health and cardiovascular disease consensus document. *European Heart Journal*
790 *Supplements*, 2010;12:B13–B22.
- 791 Boutouyrie P, Germain DP, Tropeano AI, Laloux B, Carezni F, Zidi M, Jeunemaitre
792 X, Laurent S. Compressibility of the carotid artery in patients with pseudoxan-
793 thoma elasticum. *Hypertension*, 2001;38:1181–1184.
- 794 Cheng DC, Jiang X. Detections of arterial wall in sonographic artery images using
795 dual dynamic programming. *IEEE Transactions on Information Technology in*
796 *Biomedecine*, 2008;12:792–799.
- 797 Cheng DC, Schmidt-Trucksäss A, Cheng K, Burkhardt H. Using snakes to detect the
798 intimal and adventitial layers of the common carotid artery wall in sonographic
799 images. *Computer Methods and Programs in Biomedicine*, 2002;67:27–37.
- 800 Chuong C, Fung Y. Compressibility and constitutive equation of arterial wall in
801 radial compression experiments. *Journal of biomechanics*, 1984;17:35–40.
- 802 Faita F, Gemignani V, Bianchini E, Giannarelli C, Ghiadoni L, Demi M. Real-time
803 measurement system for evaluation of the carotid intima-media thickness with a
804 robust edge operator. *Journal of Ultrasound in Medicine*, 2008;27:1353–1361.
- 805 Ilea DE, Duffy C, Kavanagh L, Stanton A, Whelan PF. Fully automated segmen-
806 tation and tracking of the intima media thickness in ultrasound video sequences

- 807 of the common carotid artery. *Ultrasonics, Ferroelectrics, and Frequency Control*,
808 *IEEE Transactions on*, 2013;60.
- 809 Jarauta E, Mateo-Gallego R, Bea A, Burillo E, Calmarza P, Civeira F. Carotid
810 intima-media thickness in subjects with no cardiovascular risk factors. *Revista*
811 *Española de Cardiología (English Edition)*, 2010;63:97–102.
- 812 Kapellas K, Maple-Brown LJ, Jamieson LM, Do LG, O’Dea K, Brown A, Cai TY,
813 Anstey NM, Sullivan DR, Wang H, Celermajer DS, Slade GD, Skilton MR. Ef-
814 fect of periodontal therapy on arterial structure and function among aboriginal
815 australians a randomized, controlled trial. *Hypertension*, 2014;64:702–708.
- 816 Kavousi M, Elias-Smale S, Rutten JHW, Leening MJG, Vliegenthart R, Verwoert
817 GC, Krestin GP, Oudkerk M, de Maat MPM, Leebeek FWG, Mattace-Raso FUS,
818 Lindemans J, Hofman A, Steyerberg EW, van der Lugt A, van den Meiracker AH,
819 Wittteman JCM. Evaluation of newer risk markers for coronary heart disease risk
820 classification: A cohort study. *Annals of Internal Medicine*, 2012;156:438–444.
- 821 Lee YB, Choi YJ, Kim MH. Boundary detection in carotid ultrasound images using
822 dynamic programming and a directional haar-like filter. *Computers in Biology and*
823 *Medicine*, 2010;40:687–697.
- 824 Li H, Yezzi A. Vessels as 4D curves: Global minimal 4D paths to extract 3D tubular
825 surfaces and centerlines. *IEEE Transactions on Medical Imaging*, 2007;26:1213–
826 1223.
- 827 Liang Q, Wendelhag I, Wikstrand J, Gustavsson T. A multiscale dynamic program-
828 ming procedure for boundary detection in ultrasonic artery images. *IEEE Trans-*
829 *actions on Medical Imaging*, 2000;19:127–142.
- 830 Loizou CP. A review of ultrasound common carotid artery image and video segmen-
831 tation techniques. *Medical & Biological Engineering & Computing*, 2014;52:1073–
832 1093.
- 833 Loizou CP, Pattichis CS, Pantziaris M, Tyllis T, Nicolaides A. Snakes based segmen-
834 tation of the common carotid artery intima media. *Medical & Biological Engineer-*
835 *ing & Computing*, 2007;45:35–49.
- 836 Lorenz MW, Markus HS, Bots ML, Rosvall M, Sitzer M. Prediction of clinical car-
837 diovascular events with carotid intima-media thickness: a systematic review and
838 meta-analysis. *Circulation*, 2007;115:459–467.

- 839 Mao F, Gill J, Downey D, Fenster A. Segmentation of carotid artery in ultra-
840 sound images: Method development and evaluation technique. *Medical Physics*,
841 2000;27:1961–1970.
- 842 Meinders JM, Kornet L, Hoeks APG. Assessment of spatial inhomogeneities in intima
843 media thickness along an arterial segment using its dynamic behavior. *American*
844 *Journal of Physiology-Heart and Circulatory Physiology*, 2003;285:H384–H391.
- 845 Menchón-Lara RM, Bastida-Jumilla MC, Morales-Sánchez J, Sancho-Gómez JL. Au-
846 tomatic detection of the intima-media thickness in ultrasound images of the com-
847 mon carotid artery using neural networks. *Medical & Biological Engineering &*
848 *Computing*, 2014;52:169–181.
- 849 Metz CT, Klein S, Schaap M, van Walsum T, Niessen WJ. Nonrigid registration of
850 dynamic medical imaging data using nD+t B-splines and a groupwise optimization
851 approach. *Medical Image Analysis*, 2011;15:238–249.
- 852 Molinari F, Zeng G, Suri JS. A state of the art review on intima-media thick-
853 ness (IMT) measurement and wall segmentation techniques for carotid ultrasound.
854 *Computer Methods and Programs in Biomedicine*, 2010;100:201–221.
- 855 Molinari F, Zeng G, Suri JS. Completely automated robust edge snapper for carotid
856 ultrasound imt measurement on a multi-institutional database of 300 images. *Med-*
857 *ical & Biological Engineering & Computing*, 2011;49:177–192.
- 858 O’Leary DH, Polak JF, Kronmal RA, Manolio TA, Burke GL, Wolfson Jr SK.
859 Carotid-artery intima and media thickness as a risk factor for myocardial infarction
860 and stroke in older adults. *New England Journal of Medicine*, 1999;340:14–22.
- 861 Polak JF, Johnson C, Harrington A, Wong Q, O’Leary DH, Burke G, Yanez
862 ND. Changes in carotid intima-media thickness during the cardiac cycle: The
863 multi-ethnic study of atherosclerosis. *Journal of the American Heart Association*,
864 2012a;1.
- 865 Polak JF, Meisner A, Pencina MJ, Wolf PA, D’Agostino RB. Variations in common
866 carotid artery intima-media thickness during the cardiac cycle: implications for
867 cardiovascular risk assessment. *Journal of the American Society of Echocardiogra-*
868 *phy*, 2012b;25:1023–1028.
- 869 Polak JF, Pencina MJ, Pencina M, O’Donnell CJ, Wolf PA, D’Agostino Sr RB.
870 Carotid-wall intima–media thickness and cardiovascular events. *New England*
871 *Journal of Medicine*, 2011;365:213–221.

- 872 Rocha R, Campilho A, Silva J, Azevedo E, Santos R. Segmentation of the carotid
873 intima-media region in B-mode ultrasound images. *Image and Vision Computing*,
874 2010;28:614–625.
- 875 Selzer RH, Mack WJ, Lee PL, Kwong-Fu H, Hodis HN. Improved common carotid
876 elasticity and intima-media thickness measurements from computer analysis of
877 sequential ultrasound frames. *Atherosclerosis*, 2001;154:185–193.
- 878 Skilton MR, Boussel L, Bonnet F, Bernard S, Douek PC, Moulin P, Serusclat A.
879 Carotid intima-media and adventitial thickening: Comparison of new and es-
880 tablished ultrasound and magnetic resonance imaging techniques. *Atherosclerosis*,
881 2011;215:405–410.
- 882 Touboul PJ, Hennerici MG, Meairs S, Adams H, Amarenco P, Bornstein N, Csiba L,
883 Desvarieux M, Ebrahim S, Hernandez Hernandez R, Jaff M, Kownator S, Naqvi T,
884 Prati P, Rundek T, Sitzler M, Schminke U, Tardif JC, Taylor A, Vicaut E, Woo KS.
885 Mannheim Carotid Intima-Media Thickness and Plaque Consensus (2004–2006–
886 2011): An Update on Behalf of the Advisory Board of the 3rd and 4th Watching
887 the Risk Symposium 13th and 15th European Stroke Conferences, Mannheim, Ger-
888 many, 2004, and Brussels, Belgium, 2006. *Cerebrovascular Diseases*, 2012;34:290–
889 296.
- 890 Truijman MTB, Kooi ME, Dijk AC, Rotte AAJ, Kolk AG, Liem MI, Schreuder
891 FHBM, Boersma E, Mess WH, Oostenbrugge RJ, Koudstaal PJ, Kappelle LJ,
892 Nederkoorn PJ, Nederveen AJ, Hendrikse J, van der Steen AFW, Daemen MJAP,
893 van der Lugt A. Plaque At RISK (PARISK): prospective multicenter study to
894 improve diagnosis of high-risk carotid plaques. *International Journal of Stroke*,
895 2014;9:747–754.
- 896 WHO. World Health Organization, Cardiovascular diseases (CVDs), Fact sheet num-
897 ber 317, 2015.
- 898 Wink O, Niessen WJ, Viergever M. Multiscale vessel tracking. *Medical Imaging*,
899 *IEEE Transactions on*, 2004;23:130–133.
- 900 Xu X, Zhou Y, Cheng X, Song E, Li G. Ultrasound intima-media segmentation
901 using Hough transform and dual snake model. *Computerized Medical Imaging*
902 *and Graphics*, 2012;36:248–258.
- 903 Zahnd G, Orkisz M, Sérusclat A, Moulin P, Vray D. Evaluation of a Kalman-based
904 block matching method to assess the bi-dimensional motion of the carotid artery
905 wall in B-mode ultrasound sequences. *Medical Image Analysis*, 2013a;17:573–585.

- 906 Zahnd G, Orkisz M, Sérusclat A, Moulin P, Vray D. Simultaneous extraction of
907 carotid artery intima-media interfaces in ultrasound images: assessment of wall
908 thickness temporal variation during the cardiac cycle. *International Journal of*
909 *Computer Assisted Radiology and Surgery*, 2013b;9:645–658.
- 910 Zahnd G, Vray D, Sérusclat A, Alibay D, Bartold M, Brown A, Durand M, Jamieson
911 LM, Kapellas K, Maple-Brown LJ, O’Dea K, Moulin P, Celermajer DS, Skilton
912 MR. Longitudinal displacement of the carotid wall and cardiovascular risk factors:
913 associations with aging, adiposity, blood pressure and periodontal disease inde-
914 pendent of cross-sectional distensibility and intima-media thickness. *Ultrasound*
915 *in Medicine & Biology*, 2012;38:1705–1715.